

# We are IntechOpen, the world's leading publisher of Open Access books Built by scientists, for scientists

6,900

Open access books available

185,000

International authors and editors

200M

Downloads

Our authors are among the

154

Countries delivered to

TOP 1%

most cited scientists

12.2%

Contributors from top 500 universities



WEB OF SCIENCE™

Selection of our books indexed in the Book Citation Index  
in Web of Science™ Core Collection (BKCI)

Interested in publishing with us?  
Contact [book.department@intechopen.com](mailto:book.department@intechopen.com)

Numbers displayed above are based on latest data collected.  
For more information visit [www.intechopen.com](http://www.intechopen.com)



# Tensile Mechanical Properties and Failure Behaviors of Friction Stir Processing (FSP) Modified Mg-Al-Zn and Dual-Phase Mg-Li-Al-Zn Alloys

Chung-Wei Yang

Additional information is available at the end of the chapter

<http://dx.doi.org/10.5772/54313>

## 1. Introduction

With the gradually depletion of natural resources, especially for the petrochemical fuel in the Earth, and the global warming problems, the energy-saving, increasing fuel-efficiency and eco-technologies have become worldwide interested subjects of nowadays. Recently, alternative green energies, such as solar energy/cells, fuel cells, Li-ion batteries, biomass fuel and algae fuel, have been developed and used as eco-friendly energies. In addition, materials chosen to give high performance in use with minimized impact to the environment during manufacture and delivery is another important concept to take into consideration. For the purpose of reducing fuel consumption, therefore, lightweight metallic materials are generally applied to replace traditional ferrous structural metals in the transportation vehicles

The definition of “Light metals” has typically been given to metallic materials with which density less than  $4.5 \text{ g cm}^{-3}$ . On this basis, the alkali metals for lithium (Li,  $0.54 \text{ g cm}^{-3}$ ), sodium (Na,  $0.97 \text{ g cm}^{-3}$ ), potassium (K,  $0.86 \text{ g cm}^{-3}$ ), rubidium (Rb,  $1.53 \text{ g cm}^{-3}$ ), cesium (Cs,  $1.9 \text{ g cm}^{-3}$ ), and alkaline earth metals for beryllium (Be,  $1.85 \text{ g cm}^{-3}$ ), magnesium (Mg,  $1.74 \text{ g cm}^{-3}$ ), calcium (Ca,  $1.55 \text{ g cm}^{-3}$ ), strontium (Sr,  $2.63 \text{ g cm}^{-3}$ ), barium (Ba,  $3.51 \text{ g cm}^{-3}$ ) can be thought of light metals. In addition, the core group of metals, such as aluminum (Al,  $2.7 \text{ g cm}^{-3}$ ) and titanium (Ti,  $4.5 \text{ g cm}^{-3}$ ), are also classed as light metals. Considering for the engineering applications of these metals in structural components, Mg, Al, Ti metals and their alloys are the generally recognized as light metals in industrial applications with respect to other engineering alloys because the specific strength (i.e., a strength-to-density ratio) is an important factor to be concerned with the weight reduction. The advantages of decreased density become important in engineering design when mechanical properties of stiffness

and resistance to buckling are involved. Comparative stiffness for equal weights of a similar beam increase in the ratios 1:2.9:8.2:18.9 for steel, Ti, Al and Mg, respectively.

Lightweight magnesium (Mg), which has the lowest density ( $1.74 \text{ g cm}^{-3}$ ) of any metallic constructional material in industrial applications [1,2]. It has many advantages such as high specific strength, high specific stiffness, well recyclability and radiation absorption of electromagnetic waves. It also provides high damping capacities, high thermal and electrical conductivities [1,3]. These effects combine to make Mg alloy be an efficient heat sink with good noise and vibration reduction properties. Researches and developments of Mg and its alloys are expanded during the past decade. They are now widely used in consumer electronic industries, biomedical and sports applications. There are numerous applications within the automobiles and aerospace [4,5] of nowadays for the purpose of reducing vehicle weight and fuel consumption [1,6,7]. However, the more widespread commercial applications of Mg alloys are limited due to its poor formability at room temperature arising from its hexagonal close-packed (hcp) crystal structure. Therefore, it is important to develop the Mg alloys having excellent mechanical properties, especially for applications at elevated temperatures. Additionally, the welded structure is inevitably used in the engineering application of wrought Mg alloys. The welding of Mg alloys can be achieved by using TIG, MIG, resistance spot welding (RSW), laser beam welding [8,9] and vacuum electron beam welding [10] processes. But the Mg-based alloys are generally of poor weldability because of their exceptional thermal and electrical properties and oxidation characteristics. In 1991, a novel friction stir welding (FSW) process was invented by The Welding Institute (TWI) of UK [11]. FSW is a solid-state joining technique and the joining temperature is lower than that in the melting welding process. It uses a high speed rotating tool consisting of a pin and tool shoulder to apply frictional heat and severe plastic deformation of the base metal and to produce a reliable metallurgical joint. Compared with the traditional melting welding techniques, FSW has many advantages [12-14] and it is quite suitable for the welding of Mg alloys and other lightweight aluminum (Al) and titanium (Ti) alloys [15-19]. In recent years, numbers of researches have been conducted to evaluate the feasibility of FSW process for Mg alloys. Moreover, the joining of dissimilar metals of Mg, Al, Cu and Ti can also be easily achieved by the FSW process [20-24].

The present chapter focuses on investigating the modification effect of friction stir process (FSP) on the tensile mechanical properties and failure behaviors of Mg-Al-Zn (AZ-series) and Mg-Li-Al-Zn and LAZ-series alloys. Section 2 will give a overview for the recently researches and applications of the these Mg-based alloys and the FSW-joining/FSP-modification techniques. In section 3, extruded Mg-6Al-1Zn (AZ61) alloys with full-annealed (AZ61-O) and FSP-modified (AZ61-FSP) specimens were used for evaluating the strain rate and texture effects on the tensile properties and failure behaviors. In section 4, we focused on investigating tensile mechanical properties and failure behaviors of the  $\alpha/\beta$ -dual-phase Mg-10Li-2Al-1Zn (LAZ1021) extruded alloy. A significant ductile-to-brittle transition phenomenon was confirmed for the dual-phase Mg-Li alloy. Since the phase composition and crystallographic structure vary significantly according to Li content, it is important to investigate the mechanical properties, as well as deformation and failure behaviors of Mg-Li al-

loys with performing the FSP modification. The aim in section 5 also focuses on improving tensile mechanical properties and evaluating failure behaviors of compositional-stabilized dual-phase LAZ1021 extruded alloy through the modification of FSP technique.

## 2. Overview of magnesium-based alloys and friction stir process

### 2.1. Lightweight magnesium (Mg) alloys

Mg alloys can generally be divided into casting alloys and wrought alloys. The casting Mg alloys include die casting, sand casting and thixomolding alloys, and wrought Mg alloys are available as bars, forgings, extrusion sheets and plates. Because of the difficulty of cold working Mg alloys, the castings are more prevalent product (account for about 85-90%) of Mg alloys usage than wrought products. Die casting is one of the most effective fabrication methods and has been extensively used to produce Mg components. Mg alloys are designated by a combination of two capital letters followed by two numbers. The first two letters indicate the two major alloying elements in the alloy. The following two numbers stand for the approximate amounts (in weight percentage, wt.%) for the first and second alloying elements, respectively. The Mg alloy designation of alloying elements is indicated according to the following code: A-aluminum, B-bismuth, C-copper, D-cadmium, E-rare earth elements, F-iron, H-thorium, K-zirconium, L-lithium, M-manganese, N-nickel, P-lead, Q-silver, R-chromium, S-silicon, T-tin, W-yttrium, Y-antimony and Z-zinc. For example, the alloy AZ91 contains approximately 9 wt.% Al and 1 wt.% Zn. The present section will give an overview of the generally used Mg-Al based, Mg-Zn based alloys, Mg-Li based alloys and rare earth elements (RE)-containing Mg alloys. In addition, topics of Mg alloys applied as orthopaedic, dental implants and surface treating methods for corrosion resistance are also introduced in the end of this section.

#### 2.1.1. Mg-Al based alloys

The Mg-Al alloy system are the most popularly used Mg alloys. Aluminum (Al) is alloyed with Mg because it increases strength, castability and corrosion resistance. The addition of Al also provides solid solution strengthening by increasing the critical resolved shear stress for slip along the basal planes of Mg-Al alloys. Fig. 1(a) shows the equilibrium phase diagram of a binary Mg-Al alloy system. Since Al has a maximum solubility in Mg of 12.7 wt.% at 437°C and its solubility decreases to about 2 wt.% at room temperature, it is expected that this system can be strengthened by precipitation hardening when the addition of Al in amount greater than 6 wt.%. However, a coarse, incoherent precipitate of the  $\gamma$ -Mg<sub>17</sub>Al<sub>12</sub> phase intermetallic compound that discontinuously precipitated around grain boundaries without the formation of GP zones or intermediate metastable phase [25]. Since Mg alloys undergo creep mainly through the grain boundary sliding (GBS), the  $\gamma$ -Mg<sub>17</sub>Al<sub>12</sub> phase, which has a melting point of about 460°C, can not serve to pin grain boundaries at elevated temperatures, and then the creep resistance of Mg-Al alloys is reduced.

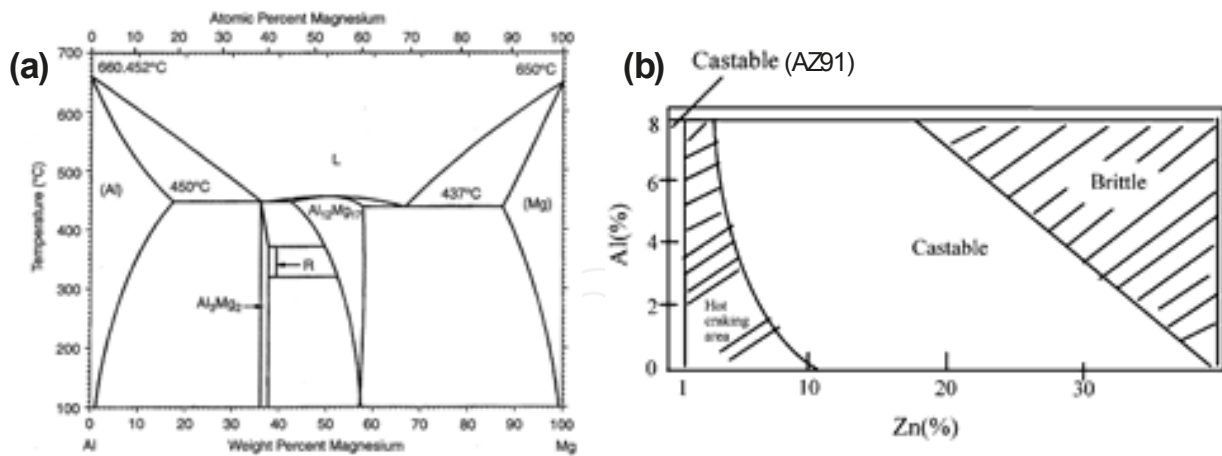


**Figure 1.** (a) Mg-Al equilibrium phase diagram, and (b) castability of the Mg-Al-Zn alloy system [26].

Zinc (Zn) is the second most important alloying elements, and the Mg-Al-Zn alloys system, which is known as the AZ-series, is the one most widely used for castings. Generally, Mg alloys are limited to a total Al and Zn content of less than 10 wt.% (the narrow region in Fig. 1(b) [26]) for obtaining good castability and weldability, whereas the hot cracking is occurred and the ductility of Mg is significantly reduced with the formation of  $\gamma$ -phase  $Mg_{17}Al_{12}$ . The castable domain of high-Zn content Mg alloys is obtained with controlling suitable Al content and the Zn/Al ratio, as shown in Fig. 1(b). When Zn is added to the Al-containing Mg alloys, it can help to refine the precipitates. It increases the strength by a combination of solid solution strengthening and precipitation hardening because Zn is approximately three times more effective than Al in increasing the yield strength for alloys that are in the solution treated and quenched condition. Zn also assists to overcome the harmful corrosive effect of iron (Fe) and nickel (Ni). For the casting Mg alloys, AZ91D is the most widely used die casting Mg alloy, and other commonly used alloys of this type are AZ81 and AZ63 alloys. AZ91D alloy offers a good room temperature mechanical properties, corrosion resistance and die castability, however, it is unsuitable for use at temperatures higher than 120°C due to its poor creep resistance. The Mg-Al and Mg-Al-Zn alloys with the addition of manganese (Mn) element are known as the AM-series alloys, such as AM60B and AM50A. They display better ductility and fracture resistant property than AZ91 alloy, and these alloys are often used for cast wheels on automobiles. Moreover, adding sufficient Mn element can help to improve the corrosion resistance by removing Fe and other heavy-metal impurities from the alloy.

Wrought Mg alloys are much less applied than castings. A relatively limited number of the AZ-series (for AZ31, AZ61 and AZ80) and ZK-series (for ZK60) alloys are used for most extrusion and forging Mg products. AZ31B is the most widely used alloy in plates and sheets. Since the room temperature formability of Mg alloys is limited, heavy deformation must be performed at above 250°C. In addition, even if wrought Mg alloys are strengthened by a combination of cold working, grain refinement and solid solution strengthening, they still relatively limited use due to the strength is much lower than medium-strength Al-Mg-Si



based alloys and the softening at elevated temperatures. Thus, the attempts to obtain high-strength wrought Mg alloys are made and some alloys have been developed [27].

### 2.1.2. Mg-Zn based alloys

Mg-Zn alloys respond to age hardening, which is associated with two intermediate precipitates of  $\beta_1'$ -MgZn<sub>2</sub> phase (rods, coherent) and  $\beta_2'$ -MgZn<sub>2</sub> phase (discs, semicoherent). The final equilibrium precipitate is  $\beta$ -Mg<sub>2</sub>Zn<sub>3</sub> phase (incoherent). Since AZ91D alloy is unsuitable for applications at elevated temperatures due to its decrease in strength and poor creep resistance [28,29], Mg-Zn-Al alloys (designated as the ZA-series) with a high Zn content is developed as a promising alloy system, which is able to improve the above requirements [29-31]. Fig. 2(a) shows the ternary phase diagram of Mg-rich Mg-Zn-Al alloy, the ternary intermetallic compounds of  $\tau$ -phase (Mg<sub>32</sub>(Al,Zn)<sub>49</sub>), Mg-rich  $\varphi$ -phase (Mg<sub>5</sub>Zn<sub>2</sub>Al<sub>2</sub>) and the binary intermetallic compound of  $\varepsilon$ -phase (MgZn) are found in the Mg-Zn-Al system. In addition, a ternary icosahedral quasi-crystalline phase, denoted as the Q-phase, is also identified in the ZA-series Mg alloys [30,32]. Zhang et al. indicated that the change of microstructural constituent of alloys is dominated by both the content of Zn, Al elements and the Zn/Al ratio [32]. As shown in Fig. 2(b), ZA-series alloys with a high Zn/Al ratio and a low Al content fall into the  $\varepsilon$ -phase, and alloys with an intermediate Zn/Al ratio and an intermediate Al content display the  $\tau$ -phase. Those alloys with a low Zn/Al ratio and a high Al content are dominated by the icosahedral quasi-crystalline Q-phase with an approximate composition of Mg<sub>9</sub>Zn<sub>4</sub>Al<sub>3</sub>, and such phase shows a short-range order of the crystalline state. Although the ZA-series alloys show a lower elongation than the AZ91, however, it is noted that the creep resistance of ZA-series alloys is significantly higher than the AZ91 alloy because no  $\gamma$ -Mg<sub>17</sub>Al<sub>12</sub> phase is formed. Moreover, the elevated temperatures creep resistance property of the  $\tau$ -type and the Q-type ZA-series alloys are superior to that of the  $\varepsilon$ -type alloys [32].

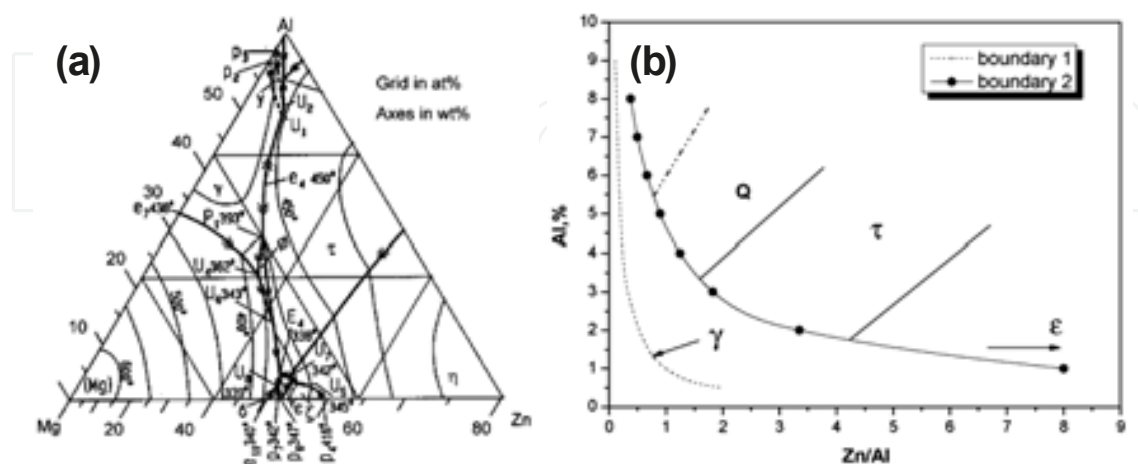


**Figure 2.** (a) Liquidus projection of the Mg-rich Mg-Zn-Al ternary phase diagram, and (b) schematic illustration of microstructural constituent as a function of the Zn/Al ratio and the Al content [32]. Boundary 1 and 2 are the two boundaries of the hot cracking area in Fig. 1(b).

The Mg-Zn alloys with the addition of zirconium (Zr) element are known as the ZK-series alloys, such as ZK51 and ZK61 casting alloys. Zr is added to Mg to reduce the harmful effects of Fe and Si elements on corrosion performance. Zr is used in casting alloys for grain refinement, and the strength of ZK-series alloys is higher than AZ-series alloys. However, they are not widely used due to they are vulnerable to microporosity during casting, and they cannot be welded for their high Zn content.

### 2.1.3. Mg-Zn-RE alloys

For aerospace and emerging automotive applications, Mg alloys with high strength, wear and creep resistance are required for engine blocks, steering wheels and transmission cases. Since the formation of low-melting  $\text{Mg}_{17}\text{Al}_{12}$  eutectic at grain boundaries sharply degrades creep resistance, the creep resistance of cast Mg-Al-based alloys will be improved when the amount of discontinuous  $\text{Mg}_{17}\text{Al}_{12}$  precipitates in grain boundary regions is reduced by adding minor elements. For example, the addition of Si can form the a new stable  $\text{Mg}_2\text{Si}$  precipitate that increase the creep strength by suppress grain boundary sliding at elevated temperatures. Reports indicated that Mg-Al-based die-cast alloys containing Ca, Sr or Si elements are now available for automotive applications [33-36]. In addition, rare earth elements (RE) containing Mg alloys exhibit improved corrosion resistance, excellent high-temperature strength and creep resistance. Therefore, the aim of recent researches is to improve the properties and broaden the structural applications of Mg alloys by alloying with RE elements. The RE elements have been shown to have a wide range of benefits for Mg alloys. It is recognized that the addition of RE elements, such as yttrium (Y), lanthanum (La), neodymium (Nd) or cerium (Ce), can improve the high temperature mechanical properties and creep strength of Mg-Al and Mg-Zn based alloys [37-46]. The Mg-Y-Nd alloys for WE54 and WE43, Mg-2.5wt.%Ag-2.0wt.%RE (QE22), Mg-RE-Zn alloys for EZ33 and EZ41 are also creep-resistant alloys which can be used for aerospace applications [47-49].

Recently, high strength Mg-Zn-RE (the alloying RE elements are Y or Gd) alloys with a long period stacking ordered (LPSO) phase were developed. The LPSO phase leads to the excellent mechanical properties. The 0.2% proof yield strength of RE-containing Mg-Zn alloys can exceed 600 MPa when they are produced by rapid solidification process [50], and a value of over 470 MPa has been obtained for the 0.2% proof yield strength in an Mg-1.8Gd-1.8Y-0.7Zn-0.2Zr alloy produced by conventional hot extrusion [51]. It is recognized that the Mg-Zn-Y alloys consisting  $\alpha$ -Mg and LPSO phases have higher strength [52,53] and superior heat resistance properties as compared to conventional Mg alloys, and the plastic deformation behavior of  $\text{Mg}_{97}\text{Zn}_1\text{Y}_2$  alloy has been investigated [54,55]. In the Mg-Zn-Gd alloys, LPSO phase precipitates from  $\alpha$ -Mg supersaturated solid solution with annealing at high temperature results in strengthening of the  $\text{Mg}_{97}\text{Zn}_1\text{Gd}_2$  alloy [56].  $\text{Mg}_{96.5}\text{Zn}_1\text{Gd}_{2.5}$  alloys with an LPSO structure exhibited high tensile yield strength (345 MPa) and large elongation (about 7%) due to the refinement of  $\alpha$ -Mg grains and the high dispersion of a hard LPSO structure phase [57]. Although Mg-Zn-RE alloys with alloy-reinforcing LPSO phase precipitates display superior mechanical properties, this two-phase structure negatively affects corrosion resistance between  $\alpha$ -Mg and LPSO phases. The corrosion resist-

ance of Mg-Zn-Y alloy can be improved with the addition of Al element, and it is expected to obtain oxide layer reforming in Mg alloys and improves corrosion resistance without changing the structure [58]. However, this Mg alloys system still require a larger quantity of adding RE elements, and the drawback is that RE elements are obtained from few sources and relatively expensive for a widespread commercial application.

#### 2.1.4. Mg-Li based alloys

Mg displays the lowest density ( $1.74 \text{ g cm}^{-3}$ ) of any constructional metal, and lithium (Li) element ( $0.53 \text{ g cm}^{-3}$ ) containing Mg-Li alloys show lower density ( $1.4\text{-}1.6 \text{ g cm}^{-3}$ ) than commonly used AZ-series and ZK-series alloys (the density is about  $1.8\text{-}1.9 \text{ g cm}^{-3}$ ). The density of Mg-Li alloys can even lower to about  $1.3 \text{ g cm}^{-3}$  when the addition of Li content is higher than 40 wt.% [59]. The Mg-Li alloys system has attracted attention as a basis for ultra-light-weight materials, which can be a good candidate for making components for aerospace vehicles [60], such as the skin of fuselage, wings and landing frame. Adding Li to Mg alloys can transform the hcp structure to a body-centered cubic (bcc) structure, substantially increasing the ductility of the Mg-Li alloys and further reducing its density [59]. According to the equilibrium Mg-Li phase diagram as shown in Fig. 3 [61], Li has a high solid solubility in Mg. When Li content is less than 5 wt.%, only Mg-rich  $\alpha$ -phase (hcp) exists. Mg alloying with the addition of about 5-11 wt.% Li content exhibits a dual-phase eutectic crystal structure, which consists of a Mg-rich  $\alpha$ -phase and a Li-rich  $\beta$ -phase (bcc). A bcc single-phase Mg-Li alloy is obtained if Li content of more than 11 wt.% is added. Mg-Li alloys have excellent formability and better vibration resistance than commonly used wrought AZ-series alloys [59,62,63]. The superplasticities of Mg-Li based alloys were also investigated [64-68]. But Mg-Li alloys exhibit low mechanical strength and they are not very useful in engineering applications. Recent studies investigated the effects of cold working, addition of alloying elements, aging and precipitation hardening on improving mechanicals of Mg-Li alloys [69-78]. Al and Zn are the commonly used elements, and Mg-Li-Al (LA-series), Mg-Li-Zn (LZ-series) and Mg-Li-Al-Zn (LAZ-series) are generally applied Mg-Li alloys. It is recognized that the precipitation of  $\theta'$ -phase ( $\text{MgLi}_2\text{X}$ ,  $\text{X} = \text{Al}$  or  $\text{Zn}$ ) in the  $\beta$ -phase results in the aging hardening effect of Mg-Li-(Al,Zn) alloys. The over aging is attributed to the precipitation of the  $\alpha$  and  $\theta$ -MgLi(Al,Zn) phases [74].

In orthopaedic and dental fields, commonly used stainless steel (e.g., ASTM F-138/139a, type 316L SS), cobalt-chromium-based alloys (e.g., ASTM F-799: Co-28Cr-6Mo, hot forged, ASTM F-562: Co-35Ni-20Cr-10Mo, cold worked and aged) and titanium-based alloys (Ti6Al4V-ELI, ASTM F-136) play an essential role as metallic biomaterials to assist with the replacement of hard tissues. However, limitations of these commonly used metallic biomaterials are the possible release of toxic metallic ions [79-81] and the stress shielding effects [82] resulted from their much higher elastic moduli than human bone tissues. Besides the applications in automotive, aerospace and electronics industry fields, Mg-based alloys have been identified as potential lightweight metallic implants in the orthopaedic field due to their high specific strength and much lower elastic modulus [83-85]. The elastic modulus of Mg alloys (about 41-45 GPa) is closer to the natural human bone (about 3-20 GPa) and much lower than com-



monly used Ti alloys (about 110 GPa) [85]. In addition, the fracture toughness of Mg alloys (about 15-40 MPa m<sup>1/2</sup>) is higher than dense HA bulks. *In vivo* studies also indicated that Mg, which is a basic element in the growth of new bone tissue, metabolism and an essential element of the enzyme system in human body [86-89], are gradually applied as biodegradable, load bearing orthopaedic implants [84]. Therefore, several Mg alloy systems, such as commonly used Mg-Al-Zn series (e.g., AZ31B and AZ91D), Mg-Ca, Mg-Zn, Mg-Zr, Mg-4wt.%Y-3wt.%RE (WE43, RE is a mixture consisting of Nd, Ce and Dy) and Mg-4wt.%Li-4wt.%Y-2wt.%RE (LAE442, RE is a mixture consisting of Ce, La and Nd) alloys [1,83-85,90-94], have been investigated and developed for using in biomedical applications in recent years. However, Mg alloys have high electrochemical activity, and the major drawback of Mg alloys in many applications is their low corrosion resistance, especially in an electrolytic aqueous environment of the human body. Thus, biomedical usage of Mg alloys is not widespread.

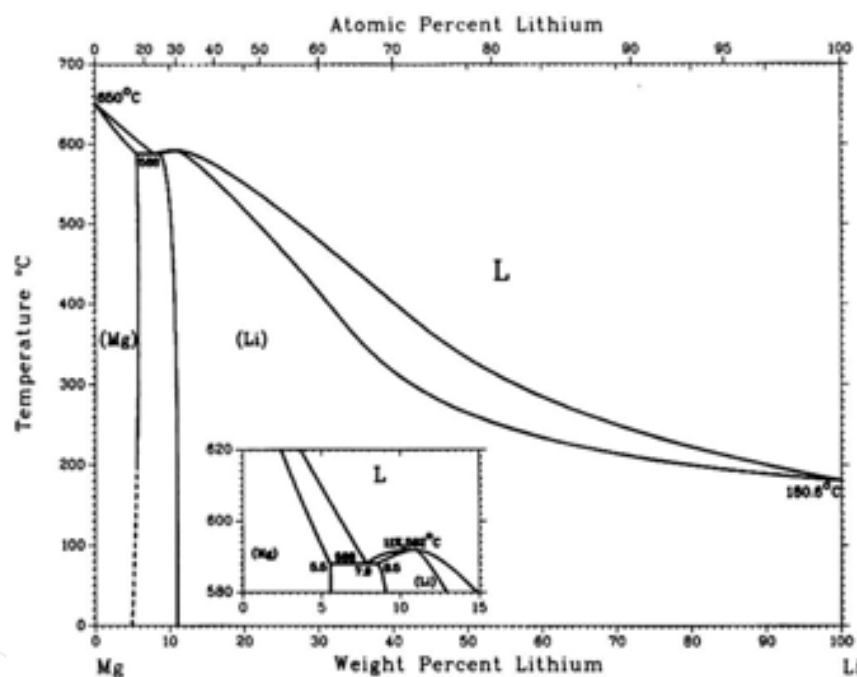


**Figure 3.** Mg-Li equilibrium phase diagram [61].

Mg alloys are susceptible to corrosion. An appropriate alloying composition can improve their mechanical properties and corrosion resistance. Mg alloys with moderate corrosion resistance and improved mechanical properties can be obtained by adding 2-10 wt.% Al with trace addition of Zn and Mn elements. The corrosion resistance and mechanical properties can also be further enhanced with adding a small amount of RE elements, such as Y, La, Nd, Ce, Zr and etc. [84]. Surface treatments, including chemical conversion coatings, anodizing, electrochemical plating, electroless nickel plating and etc. [95-97], are commonly used methods to enhance the corrosion resistance. Among these various surface treatments, the chemical conversion of Mg alloys is easier to perform for improving

corrosion resistance, and chromate conversion coatings have attracted much interest due to the simplicity of the coating process and the good corrosion resistance that offers [98]. However, environmental toxicity issues of the hexavalent chromium ( $\text{Cr}^{6+}$ ) compounds are increasingly restricting the use of the chromate bath [99,100], and Cr is also a toxic element to the human body. Thus, a  $\text{Cr}^{6+}$ -free conversion coating process is developed for the surface treatment of Mg alloys. Relative studies indicate an environmentally clean method can be achieved for synthesizing a chemical conversion coating on Mg alloys. Lin et al. [101,102] reported that an Mg,Al-hydrotalcite ( $\text{Mg}_6\text{Al}_2(\text{OH})_{16}\text{CO}_3 \cdot 4\text{H}_2\text{O}$ ) layer was developed on die cast AZ91D in an  $\text{HCO}_3^-/\text{CO}_3^{2-}$  aqueous solution to protect the alloy against corrosion. The hydrotalcite shows a crystalline structure, which has Mg,Al-layered double hydroxides ( $\text{Mg}_6\text{Al}_2(\text{OH})_{16}$ )<sup>2+</sup> intercalated by interlayers ( $\text{CO}_3 \cdot 4\text{H}_2\text{O}$ )<sup>2-</sup> [103]. It is demonstrated that the corrosion rate of Mg,Al-hydrotalcite coated specimens is evidently lower than that of the AZ91D substrate in a chloride solution [104].

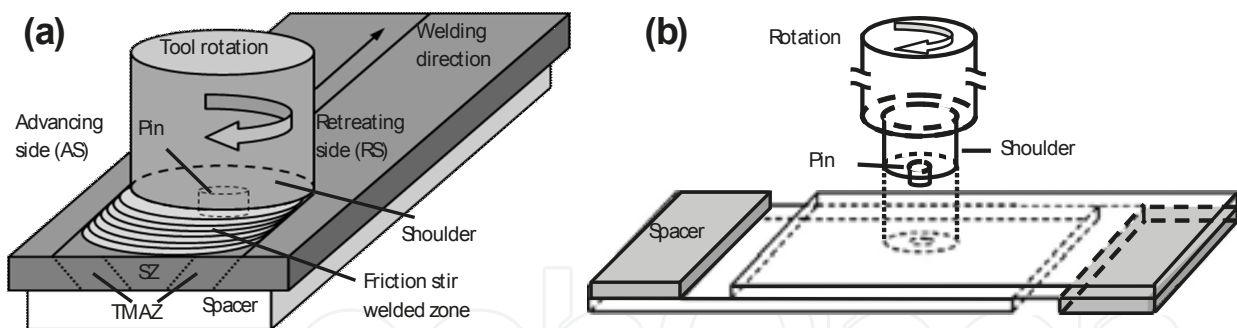
## 2.2. Friction stir welding/processing (FSW/FSP) techniques

Mg alloys can be gas welded with an oxyacetylene torch and required careful fluxing to minimize oxidation. This welding process is quite difficult, and extensive corrosion of welds is occurred when the flux is incompletely removed by the applied cleaning methods. Thus, virtually the welding of Mg alloys has been done using inert gas shielded tungsten arc welding (TIG) or consumable metal electrode arc welding (MIG) processes. In these processes, a continuously fed Mg alloy wire acts as electrode for maintaining the arc while the Ar gas shield prevents oxidation of the welds. Resistance spot welding (RSW) is applied for joining steels, Al, Mg alloys in the automotive industries of nowadays [104-108]. But RSW is relatively not suitable for joining Al or Mg alloys because of its high electrical current requirements and the inconsistent quality of final welds [109-111]. Increasing interest in using Mg alloys in aerospace and automobiles is requiring more attention to be given to alternative joining methods. Some success are achieved with the laser beam and the vacuum electron beam welding processes [8-10].

Friction stir welding (FSW) is a relatively new solid-state joining technique, which was invented by The Welding Institute (TWI) of United Kingdom in 1991 [11]. FSW can be considered as the most important development in metal joining in last decade. This joining technique is versatile, energy efficiency and environment friendly without using any cover gas and flux. It can be used to join high-strength aerospace aluminum alloys, magnesium alloys and other metallic alloys that are hard to weld by conventional fusion welding. Compared with the traditional melting welding, FSW has many advantages, and it does not need the consumable metallic wire and the protection atmosphere. FSW is quite suitable for the welding of Mg alloys because it can mitigate the susceptibility to hot cracking, compositional segregation of alloying elements and precipitation of divorced intermetallic particles. Numbers of researches have been conducted to evaluate the feasibility of FSW process for Mg alloys.

Fig. 4(a) schematically illustrates the FSW process. A non-consumable rotating tool with a specially designed pin and shoulder is plunged into the abutting edges of sheets or plates to

be joined and transversed along the welding direction (WD). The plane normal of the WD, normal direction (ND) and transverse direction (TD) are denoted in Fig 4(a). The advancing side (AS) means that the tool rotating direction is the same as the WD, and the retreating side (RS) is the inverse direction to the WD. Additionally, friction stir processing (FSP) has been developed as a thermo-mechanical microstructural modification technique of metallic materials based on the basic principles of FSW [112-114]. FSW/FSP is emerging as an effective solid-state joining/processing technique. For both FSW/FSP processes, the frictional heat is generated by the friction between the high-speed rotating tool and the workpiece. The localized heating softens of the base metals around the pin, and it causes severe plastic deformation to produce a strong metallurgical joint. This region is usually referred to as the nugget zone (or called the stir zone, SZ). The contribution of intense plastic deformation and high-temperature exposure within the SZ during FSW/FSP result in generation of a dynamically recrystallized fine-grained microstructure, development of texture, precipitate dissolution and coarsening within the SZ [114-119]. In addition, roughly positions of the thermo-mechanically affected zone (TMAZ) and the heat-affected zone (HAZ) can also be identified as indicated in Fig. 4(a) based on the microstructural characterization of grains and precipitates. The final grain size and microstructural evolution is dependent on the FSW/FSP parameters [120-122]. Many studies have been reported on the microstructural evolutions, grain refining effect, texture effect, dynamic recrystallization and mechanical properties of various Mg alloys after the FSW/FSP process [116-119,123-129].



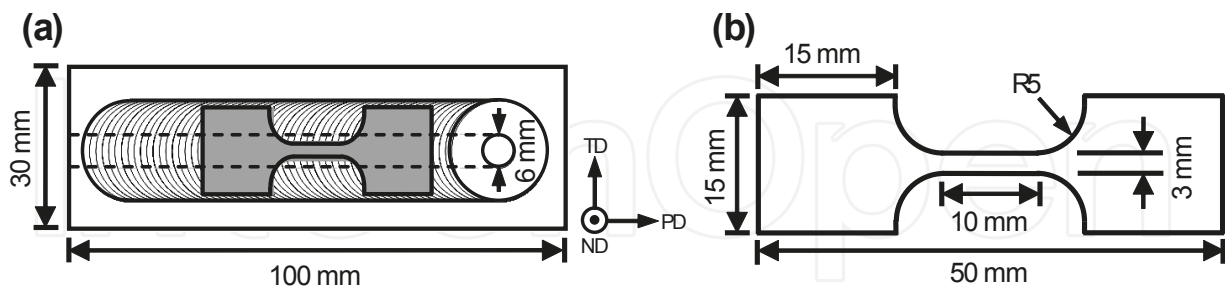
**Figure 4.** Schematic illustrations of (a) friction stir welding (FSW); (b) friction stir spot welding (FSSW).

Fig. 4(b) shows another joining type of the friction stir spot welding (FSSW), which is a derivative process of the FSW, has been developed as a widespread technique and successfully applied for producing lap-joints [130-135]. Compared with the traditional RSW process, FSSW can avoid severe heating and cooling cycles induced during welding process. Furthermore, the HAZ and residual stresses associated with the welds are relatively small [136]. Therefore, FSSW as well as FSW is now a simple and indispensable process to acquire better joining strength and vibration fracture resistance for the lightweight structural metals [130,131].

### 3. Tensile properties and failure behaviors of FSP-modified Mg-6Al-1Zn alloys

The effects of varying deformation temperature and strain rate on the microstructural features, tensile properties, deformation and failure behaviors of AZ61 Mg alloy with FSP modification are discussed in this section. The base metal is a 3 mm-thick AZ61-F extruded sheets. The sheets are full-annealed at 410°C for 20 hours, furnace cooled, and then machined into rectangular specimens with dimensions of 100 mm ( $l$ )  $\times$  30 mm ( $w$ ). The full-annealed specimens are denoted by "AZ61-O" in the following. During the FSP, a stirring pin of 6-mm diameter and 2-mm depth, protruding from a rotating rod of 20-mm diameter, is plunged into the rectangular AZ61-O specimens. The rotation speed is set at 1200 rpm, and the downward push pressure is controlled at about 22 MPa. With a tilting angle of 1.5°, the stirring pin moved along the center line of the specimens at a traverse speed of about 1 mm s<sup>-1</sup>. These specimens will be designated as "AZ61-FSP", and the plane normal of the processed direction (PD), normal direction (ND) and transverse direction (TD) are denoted in Fig. 5(a). The AZ61-O and AZ61-FSP specimens are machined into testing samples with dimensions of 50 mm ( $l$ )  $\times$  15 mm ( $w$ ). Fig. 5(a) schematically illustrates the orientation of AZ61-FSP tensile specimens, and Fig. 5(b) shows the dimensions of the tensile specimens, which gage length is completely within the stir zone (SZ).

Uniaxial tensile tests, which are conducted parallel to the PD, are performed with different initial strain rates of  $8.83 \times 10^{-3}$  s<sup>-1</sup>,  $1.67 \times 10^{-3}$  s<sup>-1</sup> and  $8.83 \times 10^{-4}$  s<sup>-1</sup> at various deformation temperatures of 200°C, 225°C and 250°C. The specimens that failed are examined using an optical microscope (OM) to observe the failure sub-surfaces on the TD plane. The micro-Vickers hardness test across the cross-section of AZ61-FSP specimen is applied using a Vickers indenter (Hv) with a 100 g load for 10 s dwell time. Each datum is the average of three tests.



**Figure 5.** Schematic illustrations of (a) the orientation of AZ61-FSP tensile specimen, (b) the tensile specimen dimension.

Fig. 6(a) shows the microstructural feature of full-annealed AZ61-O specimens. It displays equiaxed grains with an average grain size of about  $19.3 \pm 2.2$   $\mu$ m. After the FSP modification, the average grain size within the SZ of AZ61-FSP specimens is significantly refined to about  $8.2 \pm 2.5$   $\mu$ m, as shown in Fig. 6(b). It is recognized that the dynamic recrystallization

effect (DRX) governs the grain refining effect during the FSP [115]. Fig. 7 displays the microhardness (Hv) profiles along the cross-section (i.e. on the plane with a plane normal parallel to the PD) of AZ61-FSP specimen. The dash line in the micrograph represents the Vickers indenter testing area, which is located at 1 mm depth from the surface. The result shows that the microhardness within SZ (average value of Hv82.7) is increased and significantly higher than the average level of the non-stir zone (the base metal region, average value of Hv74.8).

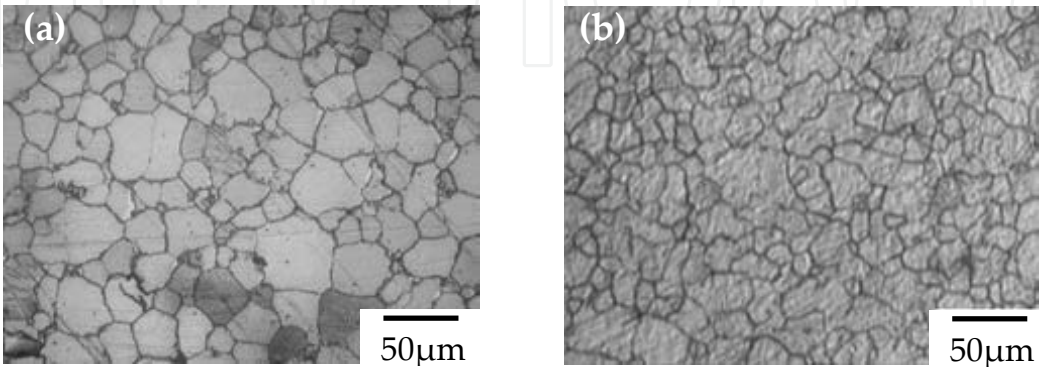


Figure 6. Optical micrograph of the (a) AZ61-O, and AZ61-FSP specimens.

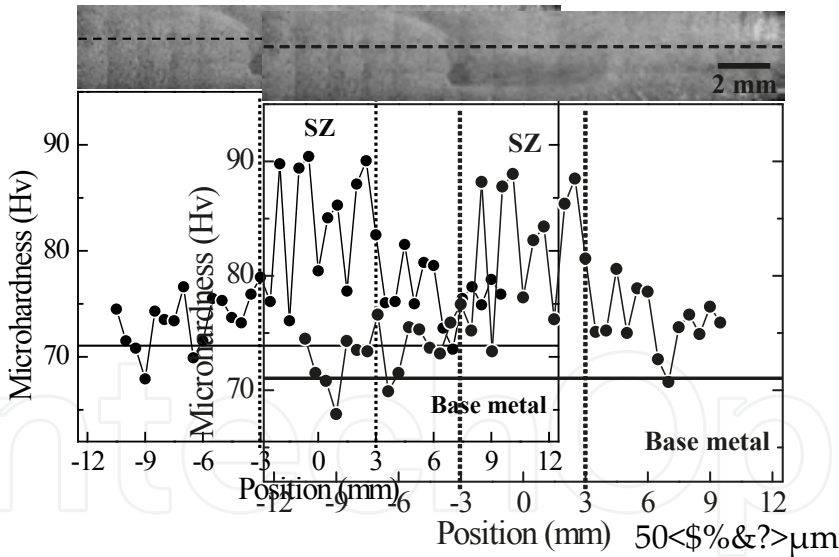


Figure 7. Microhardness (Hv) of the AZ61-FSP. The indentations are made with a spacing of 0.5 mm along the parallel dash line

3.1. Deformation temperature effect

Fig. 8 shows the stress-strain curves of the AZ61-O and AZ61-FSP specimens obtained from the uniaxial tensile tests under an initial strain rate of  $1.67 \times 10^{-3} \text{ s}^{-1}$  at various deformation

Fig. 8 shows the stress-strain curves of the AZ61-O and AZ61-FSP specimens initial strain rate of  $1.67 \times 10^{-3} \text{ s}^{-1}$  at various deformation temperatures. It can tensile strength (UTS) are decreased with increasing deformation temperature. It is noted that the total elongation (TE) is significantly increased with increasing def

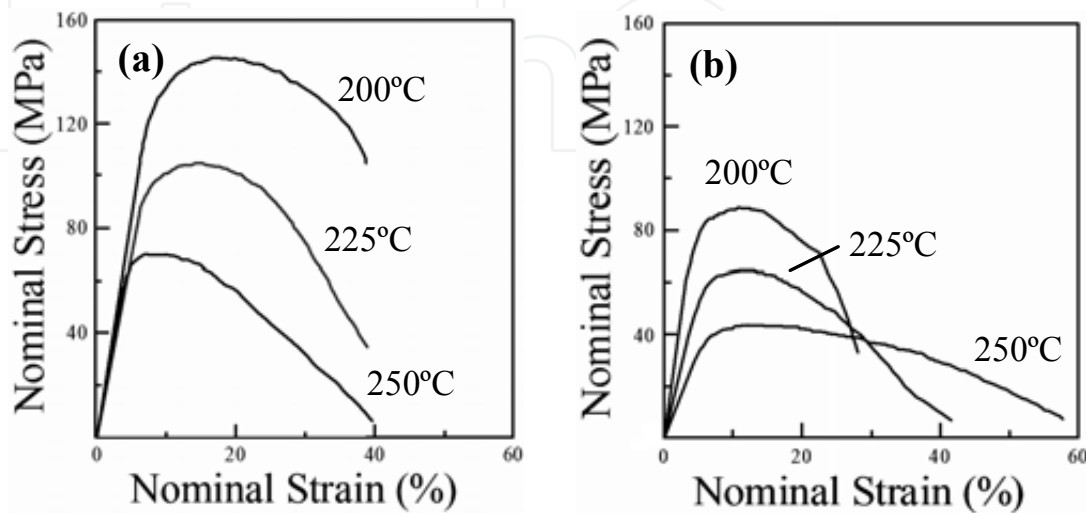




7. Microhardness (Hv) of the AZ61-FSP. The indentations are made with a spacing of 0.5 mm along parallel dash line.

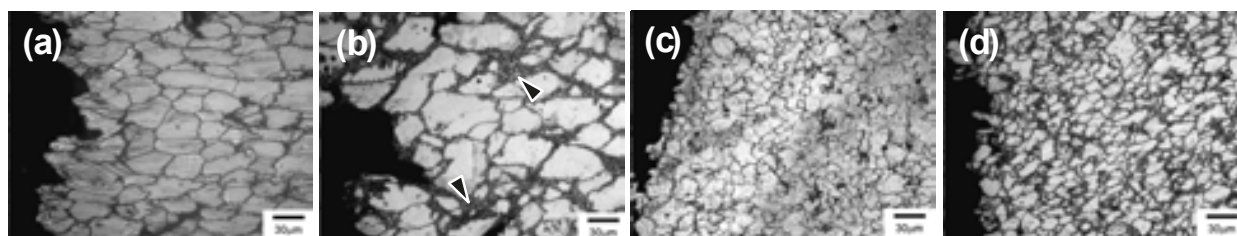
## 8. Deformation temperature effect

Fig. 8 shows the stress-strain curves of the AZ61-O and AZ61-FSP specimens obtained from the axial tensile tests under an initial strain rate of  $1.67 \times 10^{-3} \text{ s}^{-1}$  at various deformation temperatures. It can be seen that the yield strength (YS) and ultimate tensile strength (UTS) are decreased with increasing deformation temperatures for both AZ61-O and AZ61-FSP specimens. It is noted that the total elongation (TE) is significantly increased with increasing deformation temperatures for the AZ61-FSP.



8. Stress-strain curves of the (a) AZ61-O, and (b) AZ61-FSP specimens with an initial strain rate of  $1.67 \times 10^{-3} \text{ s}^{-1}$  at 200, 225 and 250°C.

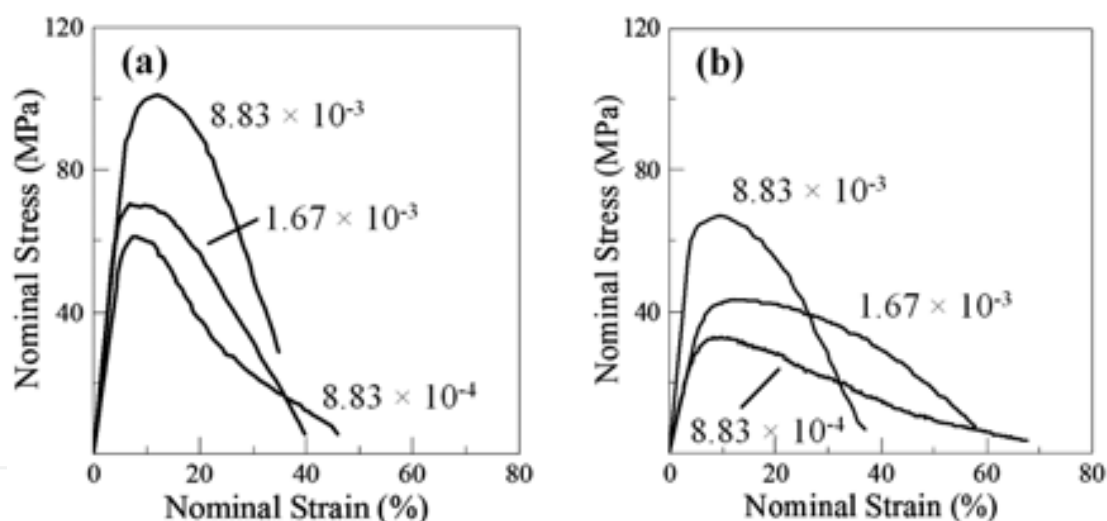
In addition, the obvious serration of stress-strain curves is observed beyond the UTS, especially for the AZ61-FSP specimens at higher deformation temperatures. This phenomenon is resulted from the dynamic recrystallization (DRX) during the tensile deformation [137,138]. Several mechanisms have been proposed for the DRX process in Mg and its alloys, such as discontinuous dynamic recrystallization (DDRX), continuous dynamic recrystallization (CDRX) and geometric dynamic recrystallization (GDRX). A CDRX process is a recovery process and proceeds by continuous absorption of dislocations in sub-grain boundaries which eventually results in the formation of high angle grain boundaries and new grains. Alternatively, DDRX, which is characterized by nucleation of new grains at original high-angle grain boundaries and nucleus growth by high-angle boundary migration [139], has been recognized as an operative mechanism for the DRX process in the SZ of FSW/FSP aluminum and magnesium alloys. Referring to the failure sub-surfaces as shown in Fig. 9(a) and 9(b), the ultra-fine new grains (as those indicated by arrows in Fig. 9(b)) nucleated and growth at the grain boundaries can be significantly recognized as the occurrence of DRX effect for AZ61-O at higher deformation temperature. From the failure sub-surfaces of AZ61-FSP as shown in Fig. 9(c) and 9(d), we can see fine-grains, which are nucleated and growth from the DRX effect, with an average grain size of about  $9 \mu\text{m}$  are formed at 200-250°C. It is recognized that the DRX effect is activated at lower temperature and the driving force of DRX is much higher for the AZ61-FSP modified specimens than the AZ61-O.



**Figure 9.** Failure sub-surfaces of AZ61-O specimen tensile tested at (a) 200°C, (b) 250°C, and AZ61-FSP specimen at (c) 200°C, (d) 250°C with an initial strain rate of  $1.67 \times 10^{-3} \text{ s}^{-1}$ .

### 3.2. Strain rate effect

Fig. 10 shows the stress-strain curves of AZ61-O and AZ61-FSP under different initial strain rates tested at 250°C. The YS and UTS are decreased, but the TE is increased with decreasing the initial strain rate. The AZ61-FSP specimens display higher TE value than AZ61-O. A significant serration of stress-strain curves is also observed beyond the UTS, especially for the AZ61-FSP specimens at lower initial strain rate.



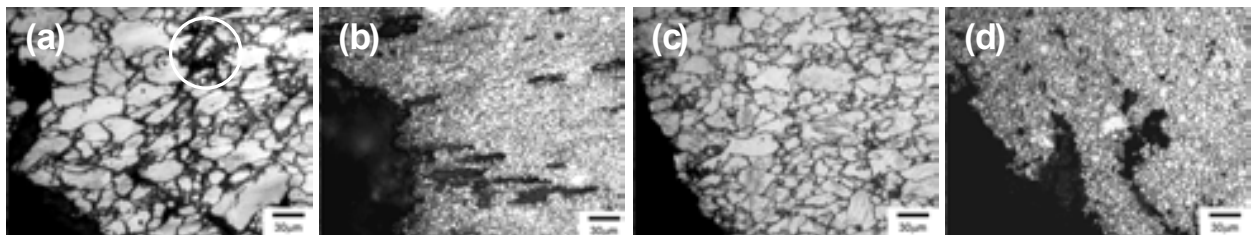
**Figure 10.** Stress-strain curves of the (a) AZ61-O, and (b) AZ61-FSP specimens with different initial strain rates of  $8.83 \times 10^{-3} \text{ s}^{-1}$ ,  $1.67 \times 10^{-3} \text{ s}^{-1}$  and  $8.83 \times 10^{-4} \text{ s}^{-1}$  at 250°C.

Fig. 11 shows the failure sub-surfaces of AZ61-O and AZ61-FSP specimens tested at 250°C for initial strain rates of  $8.33 \times 10^{-3} \text{ s}^{-1}$  and  $8.33 \times 10^{-4} \text{ s}^{-1}$  (the failure sub-surfaces of AZ61-O and AZ61-FSP for the strain rate  $1.67 \times 10^{-3} \text{ s}^{-1}$  are referred to Fig. 9(b) and 9(d), respectively). We can see that the DRX effect is occurred for both of AZ61-O (new fine-grains nucleated and growth at the grain boundaries as encircled in Fig. 11(a)) and AZ61-FSP specimens at 250°C. The DRX effect during tensile deformation is significantly occurred at relatively lower strain rate ( $8.33 \times 10^{-4} \text{ s}^{-1}$ ) because the recrystallized fine-grains are observed with an average grain size of about  $5 \mu\text{m}$  all over the microstructure, as shown in Fig. 11(b) and 11(d). Considering the AZ61-FSP specimens, the calculation of strain hardening exponent ( $n$ -val-

ue) can help to clarify the deformation mechanism of FSP-modified specimens during the DRX of tensile deformation. Fig. 12(a) shows different  $n$ -values with respect to various strain rates and deformation temperatures. The modulus  $E$  is calculated by Eq. [1], and  $T$  is for deformation temperatures in Kelvin.

$$E = 4.3 \times 10^4 \cdot [1 - 5.3 \times 10^{-4} \cdot (T - 300)] \tag{1}$$

Based on the calculation of  $n$ -value and the average grain size, the deformation mechanism of AZ61-FSP can be deduced according to the deformation mechanism map (DMM) as shown in Fig. 12(b). It is demonstrated that the grain boundary sliding (GBS) is a dominant deformation mechanism for the DRX effect during the tensile deformation performed at a lower strain rate ( $8.33 \times 10^{-4} \text{ s}^{-1}$ ) and higher deformation temperatures (at 225 and 250°C) for the AZ61-FSP specimens.



**Figure 11.** Failure sub-surfaces of AZ61-O specimen tensile tested with an initial strain rate of (a)  $8.33 \times 10^{-3} \text{ s}^{-1}$ , (b)  $8.33 \times 10^{-4} \text{ s}^{-1}$ , and AZ61-FSP specimen with (c)  $8.33 \times 10^{-3} \text{ s}^{-1}$ , (d)  $8.33 \times 10^{-4} \text{ s}^{-1}$  at 250°C.

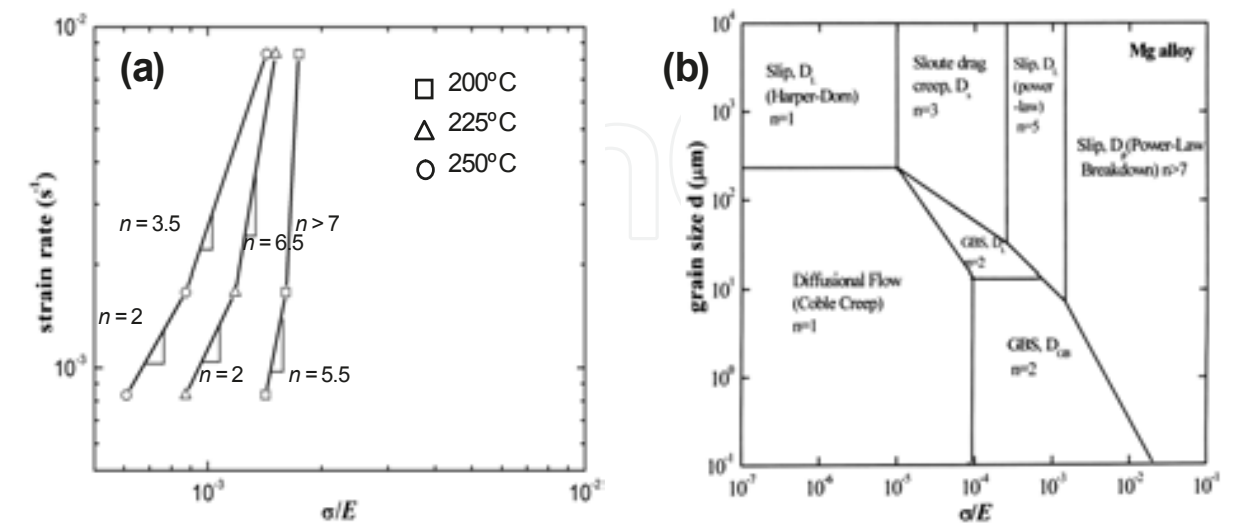


**Figure 12.** (a) The relationship between strain hardening exponent ( $n$ -value) and deformation temperatures for the AZ61-FSP at 0.2% strain, and (b) the deformation mechanism map of Mg alloy at 250°C [140].

#### 4. Tensile ductile-to-brittle transition behavior of the dual-phase Mg-Li-Al-Zn alloy

Since the phase composition and crystallographic structure vary significantly according to Li content, it is important to investigate the mechanical properties, as well as deformation and failure behaviors of Mg-Li alloys. The temperature dependence of fracturing which changes from ductile at higher temperatures to brittle at low temperatures (i.e. the ductile-to-brittle transition temperature, DBTT) is well established and occurs below room temperature for bcc metals [141-143]. The ductile-to-brittle transition has been studied in hcp Zn, Mg alloys and  $\beta$ -phase bcc Mg-Li alloy using the tensile and Charpy impact tests [75,144,145]. The Zr-based alloy with a  $\alpha/\beta$ -type dual-phase microstructure also shows ductile-to-brittle transition failure behavior [146]. Considering the variations in microstructure and mechanical properties with Li addition, it is likely that the  $\alpha/\beta$ -type dual-phase Mg-Li alloys may exhibit a transition temperature at which fracturing changes from ductile to brittle [147]. But the DBTT is seldom discussed vis-à-vis Mg alloys. This section is to investigate tensile properties at various testing temperatures and study the ductile-to-brittle transition failures for the  $\alpha/\beta$ -type Mg-Li-Al-Zn alloy.

The base metal is 3 mm-thick as-extruded Mg-10.3Li-2.4Al-0.7Zn sheets (LAZ1021). Fig. 13(a) shows the 3-D optical microstructure of the as-extruded LAZ1021 alloy, which is composed of a dual-phase crystal structure. The light gray and dark gray regions correspond to the Mg-rich  $\alpha$ -phase and the Li-rich  $\beta$ -phase, respectively. The  $\alpha$ -phase is surrounded by the  $\beta$ -phase, and the volume fraction of  $\alpha$ -phase is about 30% (vol.%). The micro-Vickers hardness test showed the average microhardness of  $\alpha$ -phase is Hv64.3, while that of  $\beta$ -phase is Hv54.0. The tensile specimen dimensions is the same as shown in Fig. 5(b). Tensile tests, which are conducted parallel to the extruded direction (ED), have an initial strain rate of  $1.67 \times 10^{-3} \text{ s}^{-1}$ . The tensile tests are performed at 25, 25, 50, 100, 150, 200 and 250°C using isothermal heating equipment. The samples that failed are examined using a SEM to observe the fracture surfaces, while the failure sub-surfaces on the TD plane are examined by an OM.

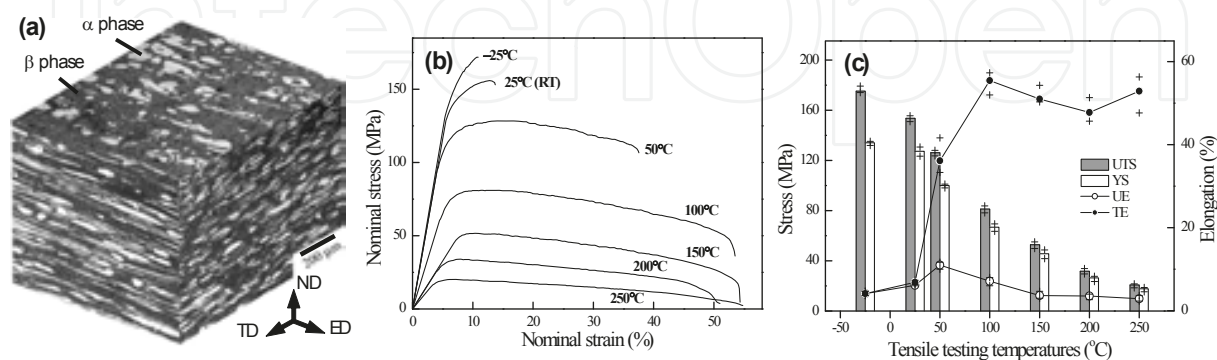


**Figure 13.** (a) Optical micrograph of as-extruded LAZ1021 base metal at the ND, ED and TD planes, (b) stress-strain curves, and (c) tensile testing results of the LAZ1021 alloy at various temperatures.



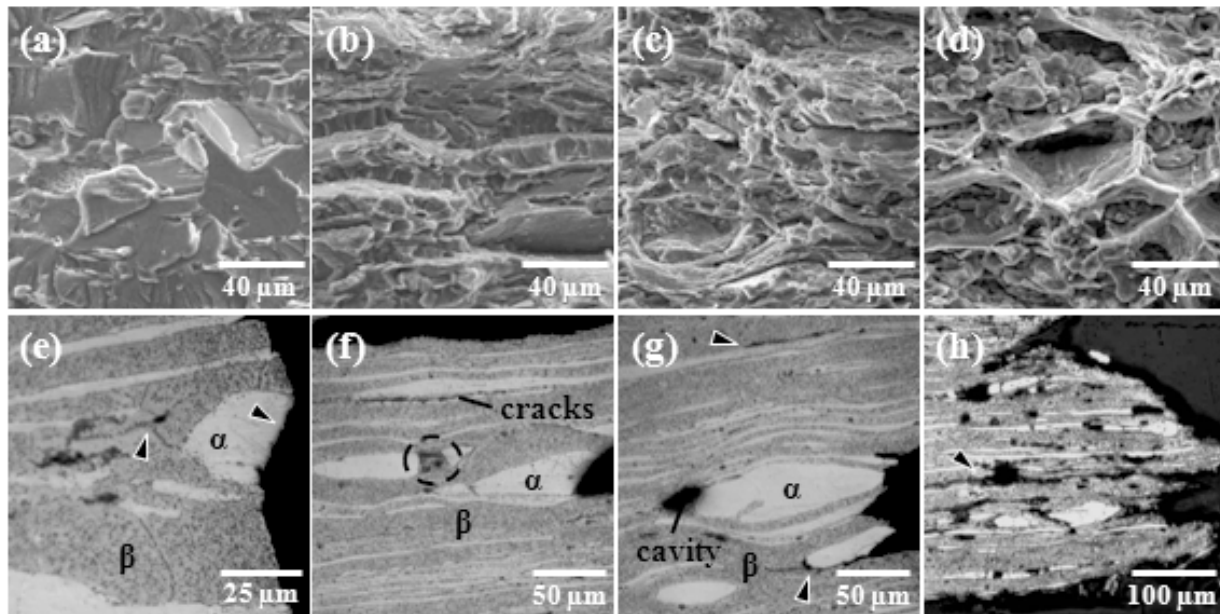
Fig. 13(b) shows the stress-strain curves of the  $\alpha/\beta$ -type LAZ1021 alloy obtained from the uniaxial tensile tests conducted with a strain rate of  $1.67 \times 10^{-3} \text{ s}^{-1}$  at various temperatures. To describe and compare the tensile properties conveniently, Fig. 13(c) displays the effect of testing temperatures on the yield strength (YS), ultimate tensile strength (UTS), uniform elongation (UE) and total elongation (TE) of the  $\alpha/\beta$  dual-phase LAZ1021 alloy. The cross markers denote the highest and the lowest values (representing the data extremes) of the measured tensile strength and elongation. It can be seen that the YS and UTS decreased with increasing deformation temperatures. The difference between YS and UTS is very small for temperatures higher than  $150^\circ\text{C}$ . It is worth noting that the elongation (especially for the TE) significantly increased at deformation temperatures higher than  $100^\circ\text{C}$ , and the ductile-to-brittle transition temperature (DBTT) can be pinpointed at about  $50^\circ\text{C}$  for the  $\alpha/\beta$ -type LAZ1021 alloy.

Fig. 14 shows the fracture surfaces and sub-surfaces (on the TD plane) within the gauge length of deformed tensile specimens for a strain rate of  $1.67 \times 10^{-3} \text{ s}^{-1}$  at certain specific deformation temperatures. Fig. 14(a) shows a brittle fracture surface, which displays a lot of cleavage features, generally observed at temperatures lower than room temperature (RT). The brittle fracturing is reduced with increasing testing temperatures, and Fig. 14(b) shows a mixed fracture surface of quasi-cleavage with tear ridges and dimpled ruptures at  $50^\circ\text{C}$ . Ductile failure with obvious dimpled ruptures appears with increasing frequency at temperatures higher than  $100^\circ\text{C}$ , as shown in Fig. 14(c) and 14(d). As seen from the fracture sub-surfaces, significant brittle fractures occurred with a mixed transgranular cleavage within  $\alpha$ -phase and grain boundary separation fracture at  $\beta$ -phase, as denoted in Fig. 14(e). Cleavage fracturing is still occurred within the  $\alpha$ -phase at a deformation temperature of  $50^\circ\text{C}$ , as shown in Fig. 14(f). However, some other  $\alpha$ -phase is clearly elongated along the tensile direction without fracture, while decohesion-induced cracking is observed at the  $\alpha/\beta$ -phase interface. Previous study indicated that cavities form easily after decohesion between the second-phase and the matrix [148]. We found that cavities appeared and the cracking at the  $\alpha/\beta$ -phase interface became more evident with increasing the deformation temperature, as denoted in Fig. 14(g). Since many of the cavities are fairly enlarged, as shown in Fig. 14(h), it is reasonable to suggest that failure occurs ultimately through cavity coalescence and interlinkage. Although the ductility of Mg-Li alloy is improved, the TE being restricted to about 55-60% can be considered as resulting from the serious cavitation and the interlinkage of cavities when specimens deformed at high temperatures. Based on the fractography, it is likely that brittle and ductile fractures are related to variations in the crystal structure and the change of slip systems.

When a metal commences to deform plastically, slip begins when the shearing stress on the slip plane in the slip direction reaches a critical resolved shear stress (CRSS). According to Schmid's law, if the tension axis is normal or parallel to the slip plane, the resolved shear stress is zero. Slip will not occur for these orientations since there is no shear stress on the slip plane. For the present used  $\alpha/\beta$ -type LAZ1021 extruded alloy, the preferred orientation of Mg-rich  $\alpha$ -phase is (0002) with a plane normal in the TD. Since the tensile direction is parallel to the basal plane, basal slip as well as the deformation twin will barely be present dur-



ing tensile tests. Brittle fracturing without significant twinning crosses through the Mg-rich  $\alpha$ -phase as shown in Fig. 14(a) and 14(e). Cleavage fracturing of the  $\alpha$ -phase generally occurs as the plastic deformation proceeds at temperatures lower than RT. In addition, brittle failure behavior can also be found in the intergranular fractures, which go along the grain boundaries within the bcc Li-rich  $\beta$ -phase, as denoted in Fig. 14(e). These phenomena cause the lack of ductility and low elongation of the  $\alpha/\beta$ -type Mg-Li-Al-Zn alloy at deformation temperatures lower than RT.



**Figure 14.** Tensile fracture surface of samples tested at (a) 25°C, (b) 50°C, (c) 100°C, (d) 250°C and failure sub-surface (at the TD plane) of samples tested at (e) 25°C, (f) 50°C, (g) 100°C and (h) 200°C.

Greater non-basal slips, including prismatic and pyramidal slip, occur in situations with a reduced  $c/a$  ratio for hcp metals (compared with the ideal value of 1.634) at elevated temperatures or when the concentration of the solid solution changes [149]. For Mg-Li-based alloys, it has been reported that the addition of Li to form a solid solution in Mg matrix will decrease the length of the  $c$ -axis and thus lead to a reduction in the  $c/a$  ratio. Research results suggest that this helps to suppress basal slip, and encourages prismatic slip. The variation in stacking fault energy should also be considered for the Mg-Li alloys. Agnew et al. [150] indicated that Li additions may lower the non-basal stacking fault energy for the glissile dislocations and increase the stability of the glissile configuration. Since the pyramidal slip mode offers five independent slip systems, it provides an explanation for the improved ductility of Mg-Li alloy. The changes in failure behavior can be attributed to variations in the  $c/a$  ratio, slip systems and stacking fault energy of the  $\alpha/\beta$ -type Mg-Li alloy.

At higher testing temperatures, we can see that the elongation significantly increased and the fraction of cleavage fracturing decreased at higher than 100°C. Since the prismatic slip of the hcp  $\alpha$ -phase is a thermally activated process and tends to be dominant above RT, lattice

twisting of hcp  $\alpha$ -phase will occur with a large number of prismatic slips; this in turn results in an increase in the mobility of basal slips during tension. Although cleavage fracturing is still likely to occur within some  $\alpha$ -phase, most of the  $\alpha$ -phase can be easily elongated, as shown in Fig. 14(f) and 14(g). The ductility of LAZ1021 alloy is significantly increased and the ductile-to-brittle transition occurs between about 50 and 100°C. Attendant with the improvement in ductility,  $\alpha/\beta$ -phase interfacial cracking, which is indicated in Fig. 14(f), begins during the ductile-to-brittle transitional interval. At testing temperatures above 100°C, cavities and  $\alpha/\beta$ -phase interfacial cracking become more obvious, as shown in Fig. 14(g) and 14(h). The cavitation and interfacial cracking may result from the elongation difference between  $\alpha$ -phase and  $\beta$ -phase. Referring to the stress-strain curves displayed in Fig. 13(b), the flow curves for 50-200°C exhibited serrations while specimens elongated beyond the UTS. Although prismatic slip and basal slip of the  $\alpha$ -phase are more active at high temperatures, deformation occurred much more easily in the bcc  $\beta$ -phase because of more slip systems. Thus, the DRX effect of the  $\beta$ -phase can be seen with refined grains as shown in Fig. 15(a). The ductile failure is due entirely to dimpled ruptures (Fig. 14(c) and 14(d), Fig. 15(b)) and resulted from the detrimental coalescence and interlinkage of cavities (Fig. 14(h)) as plane slips, DRX and  $\alpha/\beta$ -phase interfacial decohesion became more prevalent.

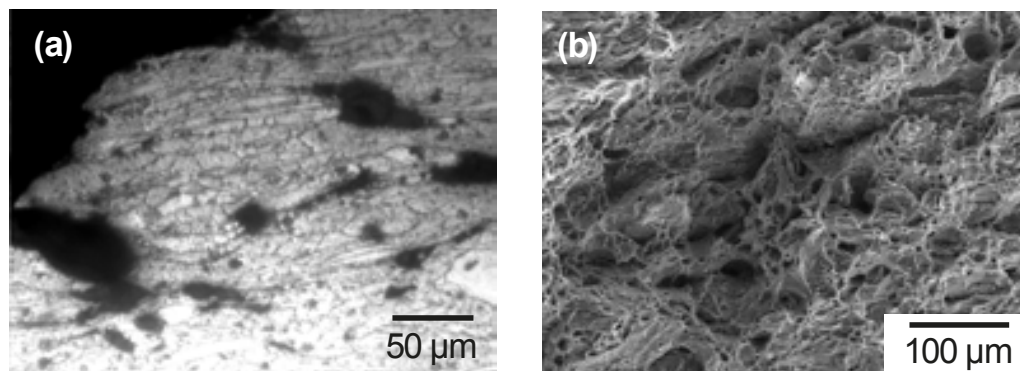


**Figure 15.** (a) The tensile failure sub-surface, and (b) the fracture surface of samples tested at 100°C.

## 5. Microstructural refining effect on mechanical properties of FSP-modified dual-phase Mg-Li-Al-Zn alloy

The aim of this section focuses on evaluating microstructural evolution, tensile mechanical properties and failure behaviors of the  $\alpha/\beta$ -dual-phase LAZ1021 extruded alloy through the modification of FSP technique. A rotating rod of 20-mm diameter with a stirring pin of 6-mm diameter and 2-mm depth is used for the FSP modification of LAZ1021. The rotation speed is set at 2500 rpm, and the downward push pressure is controlled at about 15 MPa. With a tilting angle of 1.5°, the stirring pin moved along the center line of the specimens at a traverse speed of about 2.5 mm s<sup>-1</sup>. These specimens are designated as “LAZ1021-FSP”. The phase composition and crystal structure of as-extruded LAZ1021 alloy and LAZ1021-FSP

specimens are identified by X-ray diffractometry (XRD), using  $\text{CuK}\alpha$  radiation at 30 kV, 20 mA with a scan speed of  $1^\circ (2\theta) \text{ min}^{-1}$ . XRD analysis for the texture of the LAZ1021-FSP is obtained from the stir zone (SZ) region. The micro-Vickers hardness test across the cross-section of LAZ1021-FSP specimen is applied using a Vickers indenter (Hv) with a 50 g load for 10 s dwell time. Each datum is the average of three tests. The dimension of tensile specimens, plane normal of PD, ND and TD planes are the same as defined in Fig. 5. Uniaxial tensile tests are conducted parallel to the PD with an initial strain rate of  $1.67 \times 10^{-3} \text{ s}^{-1}$  at RT. The failure sub-surfaces on the TD plane and the fracture surfaces are also examined by OM and SEM, respectively.

Fig. 16 shows the cross-sectional features of LAZ1021-FSP specimen. We can see that the microstructure is significantly changed after the FSP modification. The bottom SZ region (SZ2) displays an obvious plastic flow with a finer microstructure than the upper SZ region (SZ1), as shown in Fig. 16(a). Compared with the base metal (Fig. 16(b)), the grain size of Mg-rich  $\alpha$ -phase and Li-rich  $\beta$ -phase for the LAZ1021-FSP are refined and redistributed with an obvious texture within the SZ, as shown in Fig. 16(c) and 16(d). In addition, it is noted that the Mg-rich  $\alpha$ -phase is likely dissolved in the matrix during FSP, and then the  $\alpha$ -phase (as indicated by arrows in Fig. 16(c)) re-precipitated not only at the grain boundaries, but also within the refined grains of the  $\beta$ -phase, especially occurred in the SZ. The volume fraction of  $\alpha$ -phase is reduced to about 11–15% (vol.%) after FSP modification.

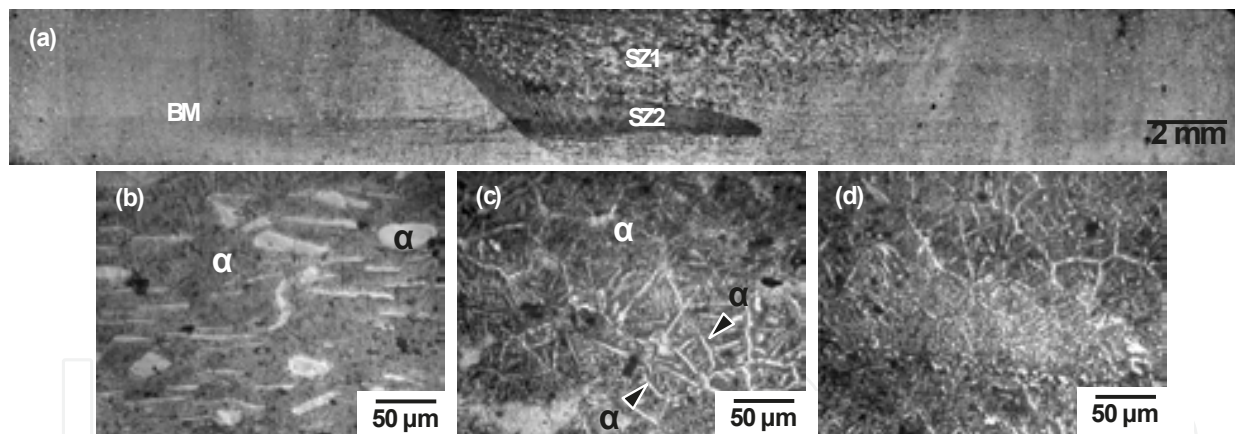


**Figure 16.** (a) The cross-sectional microstructure (on the PD plane) of the LAZ1021-FSP specimen. Microstructural features of (b) the base metal (BM), the stir zone of (c) SZ1 and (d) SZ2 denoted in (a).

Fig. 17(a) shows the XRD patterns, which display typical diffraction peaks of Mg-rich  $\alpha$ -phase and Li-rich  $\beta$ -phase, of the LAZ1021 extruded alloy on the ND, ED and TD planes. The prismatic planes of  $(11\bar{2}0)$  and  $(10\bar{1}0)$  are the preferred orientations of hcp  $\alpha$ -phase on the ND and ED planes, respectively. Some crystal planes of the  $\alpha$ -phase are also observed, though the peak intensities are low. Compared with the standard powder diffraction of Mg (JCPDS 35-0821), the  $(0002)$  basal plane, which displays a stronger peak intensity, can be recognized as the preferred orientation of the TD plane. For the hcp  $\alpha$ -phase, therefore, the basal plane is parallel to the ED, and its plane normal (the  $c$ -axis of hcp crystal structure) is



perpendicular to the TD plane. As for the bcc  $\beta$ -phase, the (200) and (110) planes are identified as the preferred orientations of the ND plane and of both the ED and TD planes, respectively. Apart from the peaks of  $\alpha$  and  $\beta$ -phases, relatively weak peaks are also observed in Fig. 17(a), and these peaks belong to the AlLi intermetallic compound (JCPDS 71-0362). Fig. 17(b) shows the XRD patterns obtained from SZ regions on the ND, PD and TD planes of the LAZ1021-FSP specimen, respectively. Diffraction peaks of the AlLi intermetallic compound is reduced, and it is recognized that the AlLi compound is dissolved after the FSP. It is noted that the peaks intensity of the hcp  $\alpha$ -phase is significantly reduced and the texture of extruded LAZ1021 alloy is changed after the FSP, especially for the ND plane of LAZ1021-FSP specimens. We can see that the preferred orientation of the hcp  $\alpha$ -phase is varied from the prismatic plane (11 $\bar{2}$ 0) to the pyramidal plane (10 $\bar{1}$ 1), and the bcc  $\beta$ -phase is varied from (200) to (110) on the ND plane. The reduction of diffraction peaks intensity for the  $\alpha$ -phase can be resulted from the decrease in the volume fraction of  $\alpha$ -phase. The (110) plane of the bcc  $\beta$ -phase can be identified as the preferred orientation for the LAZ1021-FSP modified specimens, as shown in Fig. 17(b). The reduction of diffraction peaks intensity for the  $\alpha$ -phase can be resulted from the decrease in the volume fraction of  $\alpha$ -phase. The (110) plane of the bcc  $\beta$ -phase can be identified as the preferred orientation for the LAZ1021-FSP modified specimens, as shown in Fig. 17(b).

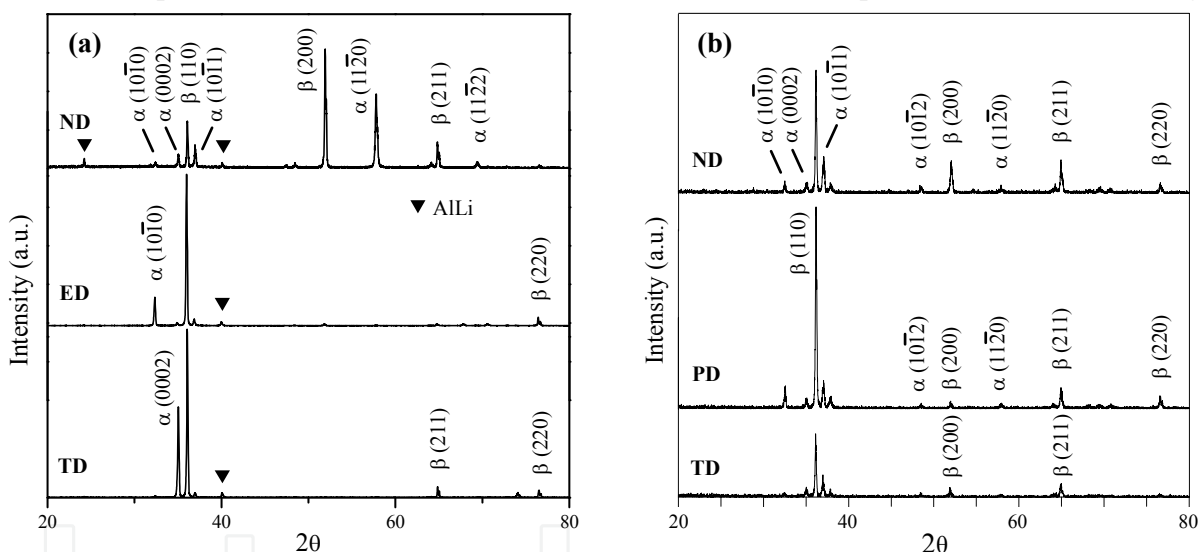


Fig. 17. X-ray diffraction patterns of (a) the as-extruded LAZ1021, and (b) the LAZ1021-FSP specimen.

**Figure 17.** X-ray diffraction patterns of (a) the as-extruded LAZ1021, and (b) the LAZ1021-FSP specimen.

Fig. 18(a) displays the microhardness (Hv) profiles along the cross-section of LAZ1021-FSP specimens. The dash line is the micrograph represents the Vickers indenter testing area, which is located at 1 mm depth from the surface. The result shows that the microhardness within SZ (average value of Hv72.5) is significantly increased and higher than the the base metal region. Fig. 18(b) displays the stress-strain curves of the as-extruded LAZ1021 alloy and the LAZ1021-FSP specimen. After FSP modification, the tensile strength is increased to about 180 MPa, but the elongation is significantly decreased for the LAZ1021-FSP specimen. The total elongation (TE) of LAZ1021 alloy is reduced from about 10% to about 3% after FSP. The variation of microhardness and tensile mechanical properties can be resulted from the microstructural features and preferred orientations (Figs. 16 and 17) are significantly varied with performing FSP modified LAZ1021. Fig. 19 shows the fracture surface and failure surface of the LAZ1021-FSP specimen. Compared with the failure morphologies of as-extruded LAZ1021 alloy (Fig. 14(a) and 14(e)), the LAZ1021-FSP specimen displays an intergranular fracture feature, as shown in Fig. 19(a). Since the  $\alpha$ -phase is precipitated at grain boundaries of the  $\beta$ -phase after FSP, it is recognized that the intergranular fracture can be resulted from the  $\alpha/\beta$ -interface decohesion and the cracks propagation along the grain boundaries of  $\beta$ -phase, as shown in Fig. 19(b).

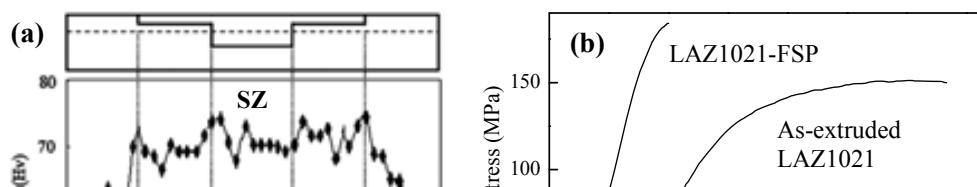


Fig. 17. X-ray diffraction patterns of (a) the as-extruded LAZ1021, and (b) the LAZ1021-FSP specimen.

Fig. 18(a) displays the microhardness (Hv) profiles along the cross-section of LAZ1021-FSP specimen. The dash line is the micrograph represents the Vickers indenter testing area, which is located at 1 mm depth from the surface. The result shows that the microhardness within SZ (average value of Hv72.5) is significantly increased and higher than the the base metal region. Fig. 18(b) displays the stress-strain curves of the as-extruded LAZ1021 alloy and the LAZ1021-FSP specimen. After FSP modification, the tensile strength is increased to about 180 MPa, but the elongation is significantly decreased for the LAZ1021-FSP specimen. The total elongation (TE) of LAZ1021 alloy is reduced from about 10% to about 3% after FSP. The variation of microhardness and tensile mechanical properties can be resulted from the microstructural features and preferred orientations (Figs. 16 and 17) are significantly varied with performing FSP modification. Fig. 19 shows the fracture surface and failure sub-surface of the LAZ1021-FSP specimen. Compared with the failure morphologies of as-extruded LAZ1021 alloy (Fig. 14(a) and 14(e)), the LAZ1021-FSP specimen displays an intergranular fracture feature, as shown in Fig. 19(a). Since the  $\alpha$ -phase is precipitated at grain boundaries of the  $\beta$ -phase after FSP, it is recognized that the intergranular fracture can be resulted from the  $\alpha/\beta$ -interface decohesion and the cracks propagation along the grain boundaries of  $\beta$ -phase, as shown in Fig. 19(b).

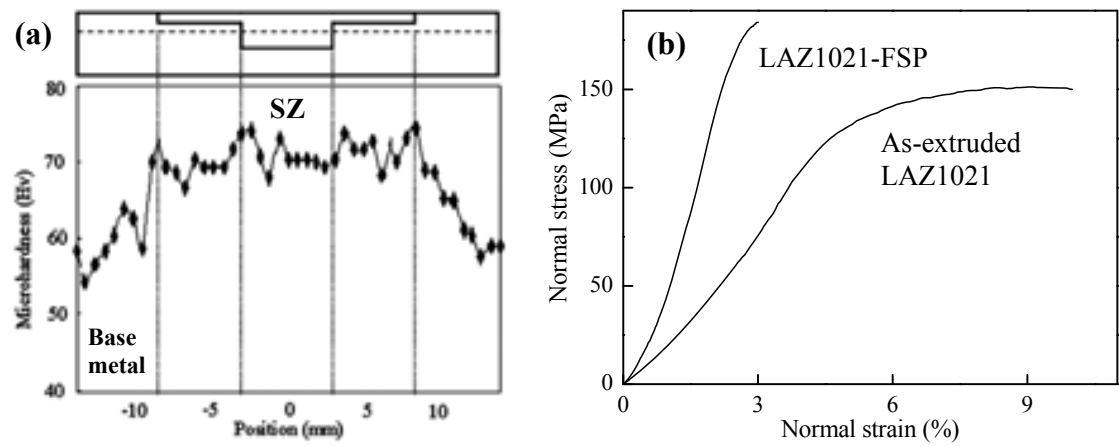


Fig. 18. (a) Microhardness (Hv) of the LAZ1021-FSP. The indentations are made with a spacing of 0.5 mm along the parallel dash line. (b) The stress-strain curves of the as-extruded LAZ1021 alloy and the LAZ1021-FSP specimen.

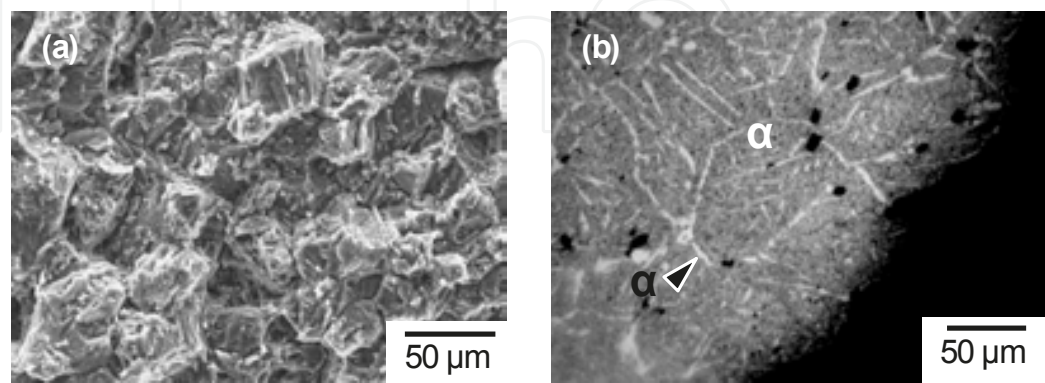


Figure 19. (a) Fracture surface, and (b) failure sub-surface on the TD plane of the LAZ1021-FSP specimen.



## 6. Conclusion

The evolution of microstructural features, tensile mechanical properties and failure behaviors of full-annealed Mg-6Al-1Zn (AZ61-O) and as-extruded  $\alpha/\beta$ -dual-phase Mg-10Li-2Al-1Zn (LAZ1021) alloys with applying a microstructural modification of the friction stir processing (FSP) are evaluated in this chapter. In summary, the grain size of AZ61-O and LAZ1021 alloys is significantly refined after the FSP modification. It is noted that the preferred orientations of hcp Mg-rich  $\alpha$ -phase and bcc Li-rich  $\beta$ -phase is changed for the LAZ1021-FSP specimens. The volume fraction of  $\alpha$ -phase is reduced after FSP, and the formation of a specific texture of the LAZ1021-FSP is resulted from the re-precipitation of  $\alpha$ -phase within the grains and at the grain boundaries of  $\beta$ -phase in the stir zone (SZ). After the FSP, the microhardness within SZ is significantly improved for both of the AZ61-O and LAZ1021 alloys.

Tensile strength is decreased and total elongation is increased with decreasing the initial strain rate for both of the AZ61-O and AZ61-FSP. The serration of tensile stress-strain curves for AZ61-FSP specimens are resulted from the dynamic recrystallization (DRX) effect. The DRX effect is activated at lower temperature and the driving force of DRX is much higher for the AZ61-FSP modified specimens than the AZ61-O. Based on the evaluation of strain hardening exponent ( $n$ -value) and average grain size, it is demonstrated that the grain boundary sliding (GBS) is a dominant deformation mechanism for the DRX during the tensile deformation performed at a lower strain rate and higher deformation temperatures for the AZ61-FSP specimens.

For  $\alpha/\beta$ -dual-phase LAZ1021 alloy, the tensile strength is increased, but the total elongation is significantly decreased after the FSP modification. LAZ1021-FSP displays an intergranular fracture, which is occurred from the  $\alpha/\beta$ -interface decohesion and crack propagation along the grain boundaries of  $\beta$ -phase. A significant ductile-to-brittle transition effect is confirmed for the  $\alpha/\beta$ -dual-phase Mg-Li-Al-Zn alloy. At temperatures lower than 25°C, fracturing occurs by transgranular cleavage of the  $\alpha$ -phase and intergranular fracture at grain boundaries of the  $\beta$ -phase. At deformation temperatures higher than 100°C, the dominant failure behaviors are interfacial cracking between  $\alpha/\beta$  interface and ductile dimpled ruptures of the  $\beta$ -phase. The ductile-to-brittle transition occurred at temperatures between 25 and 100°C, and the ductile-to-brittle transition temperature (DBTT) can be pinpointed at around 50°C for the  $\alpha/\beta$ -dual-phase LAZ1021 alloy. The dimpled rupture for specimens with higher elongation is resulted from the cavitation due to the  $\alpha/\beta$  interfacial cavities coalescence and interlinkage. Failures with dimpled ruptures occurred from the cavitation is more significant with increasing deformation temperatures.

## Acknowledgements

This study was financially supported by the National Science Council of Taiwan (Contract No. NSC 100-2221-E-150-037 and NSC 101-2221-E-150-028) for which we are grateful.

## Author details

Chung-Wei Yang

Department of Materials Science and Engineering, National Formosa University, Huwei, Yunlin, Taiwan

## References

- [1] Mordike BL, Ebert T. Magnesium properties-applications-potential. *Materials Science and Engineering A* 2001;302(1):37-45.
- [2] Eliezer D, Aghion E, Froes FH. Magnesium science technology and applications. *Advanced Performance Materials* 1998;5:201-202.
- [3] Deetz J. The use of wrought magnesium in bicycles. *JOM* 2005;57(5):50-53.
- [4] Plomear IJ. Magnesium alloys and applications. *Materials Science and Technology* 1994;10(1):1-16.
- [5] Aghion E, Bronfin B. Magnesium alloys development towards the 21th century. *Materials Science Forum* 2000;350:19-28.
- [6] VanFleteren R. Magnesium for automotive applications. *Advanced Materials and Processes* 1996;149(5):33-34.
- [7] Aghion E, Bronfin B, Eliezer D. The role of the magnesium industry in protecting the environment. *Journal of Materials Processing Technology* 2001;117:381-385.
- [8] Wang HY, Li ZJ. Investigation of laser beam welding process of AZ61 magnesium-based alloy. *Acta Metallurgica Sinica* 2006;19(4):287-294.
- [9] Padmanaban G, Balasubramanian V. Optimization of laser beam welding process parameters to attain maximum tensile strength in AZ31B magnesium alloy. *Optics & Laser Technology* 2010;42(8):1253-1260.
- [10] Luo Y, Ye H, Du C, Xu H. Influence of focusing thermal effect upon AZ91D magnesium alloy weld during vacuum electron beam welding. *Vacuum* 2012;86(9):1262-1267.
- [11] Thomas WM, Nicholas ED, Needham JC, Murch MG, Templesmith P, Dawes CJ. G. B. Patent Application, No. 9125978.8, 1991.
- [12] Mahoney MW, Rhodes CG, Flintoff JG, Bingle WH, Spurling RA. Properties of friction-stir-welded 7075-T651 aluminum. *Metallurgical and Materials Transactions A – Physical Metallurgy and Materials Science* 1998;29(7):1955-1964.
- [13] Squillace A, De Fenzo A, Giorleo G, Bellucci F. A comparison between FSW and TIG welding techniques: modification of microstructure and pitting corrosion resistance

in AA 2024-T3 butt joints. *Journal of Materials Processing Technology* 2004;152(1):97-105.

- [14] Padmanaban G, Balasubramanian V. Metallurgical characterization of pulsed current gas tungsten arc, friction stir and laser beam welded AZ31B magnesium alloy joints. *Materials Chemistry and Physics* 2011;125(3):686-697.
- [15] Wang X, Wang K. Microstructure and properties of friction stir butt-welded AZ31 magnesium alloy. *Materials Science and Engineering A* 2006;431:114-117.
- [16] Xie GM, Ma ZY, Geng L, Chen RS. Microstructural evolution and mechanical properties of friction stir welded Mg-Zn-Y-Zr alloy. *Materials Science and Engineering A* 2007;471:63-68.
- [17] Dobriyal RP, Dhindaw BK, Muthukumaran S, Mukherjee SK. Microstructure and properties of friction stir butt-welded AE42 magnesium alloy. *Materials Science and Engineering A* 2008;477(1-2):243-249.
- [18] Cerri E, Leo P. Warm and room temperature deformation of friction stir welded thin aluminum sheets. *Materials & Design* 2010;31(3):1392-1402.
- [19] Fratini L, Micari F, Buffa G, Ruisi VF. A new fixture for FSW processes of titanium alloys. *CIRP Annals – Manufacturing Technology* 2010;59(1):271-274.
- [20] Somasekharan AC, Murr LE. Microstructures in friction-stir welded dissimilar magnesium alloys and magnesium alloys to 6061-T6 aluminum alloy. *Materials Characterization* 2004;52(1):49-64.
- [21] Yan Y, Zhang DT, Qiu C, Zhang W. Dissimilar friction stir welding between 5052 aluminum alloy and AZ31 magnesium alloy. *Transactions of Nonferrous Metals Society of China* 2010;20(2):s619-s623.
- [22] Xue P, Ni DR, Wang D, Xiao BL, Ma ZY. Effect of friction stir welding parameters on the microstructure and mechanical properties of the dissimilar Al-Cu joints. *Materials Science and Engineering A* 2011;528(13-14):4683-4689.
- [23] Anouma M, Nakata K. Effect of alloying elements on interface microstructure of Mg-Al-Zn magnesium alloys and titanium joint by friction stir welding. *Materials Science and Engineering B* 2009;161(1-3):46-49.
- [24] Anouma M, Nakata K. Dissimilar metal joining of ZK60 magnesium alloy and titanium by friction stir welding. *Materials Science and Engineering B* 2012;177(7):543-548.
- [25] Clark JB. Age hardening in a Mg-9wt.%Al alloy. *Acta Metallurgica* 1968;16(2):141-152.
- [26] Foerster GS. Proceeding of the IMA 33rd Annual Meeting, May 23-25, 1976, Montreal, Quebec, Canada, p.35-39.
- [27] Hono K, Mendis CL, Sasaki TT, Oh-ishi K. Towards the development of heat-treatable high-strength wrought Mg alloys. *Scripta Materialia* 2010;63:710-715.

- [28] Miller WK. Creep of die cast AZ91 magnesium at room temperature and low stress. *Metallurgical and Materials Transactions A – Physical Metallurgy and Materials Science* 1991;22(4):873-877.
- [29] Luo A, Pekguleryuz MO. Cast magnesium alloys for elevated temperature applications. *Journal of Materials Science* 1994;29(20):5259-5271.
- [30] Zhang J, Li ZS, Guo ZX, Pan FS. Solidification microstructural constituent and its crystallographic morphology of permanent-mold-cast Mg-Zn-Al alloys. *Transactions of Nonferrous Metals Society of China* 2006;16:452-458.
- [31] Xiao W, Jia S, Wang J, Wu Y, Wang L. Effects of cerium on the microstructure and mechanical properties of Mg-20Zn-8Al alloy. *Materials Science and Engineering A* 2008;474:317-322.
- [32] Zhang J, Guo ZX, Pan F, Li Z, Luo X. Effect of composition on the microstructure and mechanical properties of Mg-Zn-Al alloys. *Materials Science and Engineering A* 2007;456(1-2):43-51.
- [33] Pekguleryuz MO, Baril E. Creep resistant magnesium diecasting alloys based on alkaline earth elements. *Materials Transactions* 2001;42(7):1258-1367.
- [34] Luo AA, Powell BR, Balogh MP. Creep and microstructure of magnesium-aluminum-calcium based alloys. *Metallurgical and Materials Transactions A – Physical Metallurgy and Materials Science* 2002;33(3):567-574.
- [35] Luo AA. Recent magnesium alloy development for elevated temperature applications. *International Materials Reviews* 2004;49(1):13-30.
- [36] Saddock ND, Suzuki A, Jones JW, Pollock TM. Grain-scale creep processes in Mg-Al-Ca base alloys: Implications for alloy design. *Scripta Materialia* 2010;63:692-697.
- [37] Lu YZ, Wang QD, Zeng XQ. Effects of rare earths on the microstructure, properties and fracture behavior of Mg-Al alloys. *Materials Science and Engineering A* 2000;278(1-2):66-76.
- [38] Zhou HT, Zhang XQ, Ding WJ, Ma CJ, Zhu YP. Effect of La and Nd on microstructures and mechanical properties of AZ61 wrought magnesium alloy. *Transactions of Nonferrous Metals Society of China* 2004;14(1):67-70.
- [39] Wang MX, Zhou H, Wang L. Effect of yttrium and cerium addition on microstructure and mechanical properties of AM50 magnesium alloy. *Journal of Rare Earths* 2007;25(2):233-237.
- [40] Zhang J, Wang J, Qiu X, Zhang D, Tian Z, Niu X, Tang D, Meng J. Effect of Nd on the microstructure, mechanical properties and corrosion behavior of die-cast Mg-4Al-based alloy. *Journal of Alloys and Compounds* 2008;464(1-2):556-564.
- [41] Pan FS, Chen MB, Wang JF, Peng J, Tang AT. Effect of yttrium addition on microstructure and mechanical properties of as-extruded AZ31 magnesium alloys. *Transactions of Nonferrous Metals Society of China* 2008;18:s1-s6.

- [42] Zhang J, Liu K, Fang D, Qiu X, Tang D, Meng J. Microstructure, tensile properties and creep behavior of high pressure die-cast Mg-4Al-4RE-0.4Mn (RE=La, Ce) alloys. *Journal of Materials Science* 2009;44(8):2046-2054.
- [43] Kaveh MA, Afshin M, Farzad K. The effect of different rare earth elements content on microstructure, mechanical and wear behavior of Mg-Al-Zn alloy. *Materials Science and Engineering A* 2010;527(7-8):2027-2035.
- [44] Tong G, Liu H, Liu Y. Effect of rare earth additions on microstructure and mechanical properties of AZ91 magnesium alloys. *Transactions of Nonferrous Metals Society of China* 2010;20:s336-s340.
- [45] Zou H. Effect of microstructure on creep behavior Mg-5%Zn-2%Al (-2%Y) alloy. *Transactions of Nonferrous Metals Society of China* 2008;18(3):580-587.
- [46] Xiao W, Jia S, Wang L, Wu Y, Wang L. The microstructure and mechanical properties of Mg-Zn-Al-RE alloys. *Journal of Alloys and Compounds* 2009;480(2):L33-L36.
- [47] Wei LY, Dunlop GL, Westengen H. Age hardening and precipitation in a cast magnesium-rare-earth alloy. *Journal of Materials Science* 1996;31(2):387-397.
- [48] Nie JF, Muddle BC. Characterization of strengthening precipitate phases in a Mg-Y-Nd alloy. *Acta Materialia* 2000;48(8):1691-1703.
- [49] Smola B., Stulikova I., Pelcova J., Mordike L. Magnesium Alloys and Their Applications. In: Kainer K.U. (ed.) Wiley-VCH Verlag, Weinheim; 2003, p43.
- [50] Kawamura Y, Hayashi K, Inoue A, Masumoto T. Rapid solidified powder metallurgy Mg<sub>97</sub>Zn<sub>1</sub>Y<sub>2</sub> alloys with excellent tensile yield strength above 600 MPa. *Materials Transactions* 2001;42(7):1172-1176.
- [51] Homma T, Kunito N, Kamado S. Fabrication of extraordinary high-strength magnesium alloy by hot extrusion. *Scripta Materialia* 2009;61(6):644-647.
- [52] Hagihara K, Kinoshita A, Sugino Y, Yamasaki M, Kawamura Y, Yasuda HY, Umakoshi Y. Effect of long-period stacking ordered phase on mechanical properties of Mg<sub>97</sub>Zn<sub>1</sub>Y<sub>2</sub> extruded alloy. *Acta Materialia* 2010;58(19):6282-6293.
- [53] Yamasaki M, Hashimoto K, Hagihara K, Kawamura Y. Effect of multimodal microstructure evolution on mechanical properties of Mg-Zn-Y extruded alloy. *Acta Materialia* 2011;59(9):3646-3658.
- [54] Matsuda M, Ii S, Kawamura Y, Ikuhara Y, Nishida M. Interaction between long period stacking order phase and deformation twin in rapidly solidified Mg<sub>97</sub>Zn<sub>1</sub>Y<sub>2</sub> alloy. *Materials Science and Engineering A* 2004;386(1-2):447-452.
- [55] Hagihara K, Kinoshita A, Sugino Y, Yamasaki M, Kawamura Y, Yasuda HY, Umakoshi Y. Plastic deformation behavior of Mg<sub>97</sub>Zn<sub>1</sub>Y<sub>2</sub> extruded alloys. *Transactions of Nonferrous Metals Society of China* 2010;20(7):1259-1268.



- [56] Yamasaki M, Sasaki M, Nishijima M, Hiraga K, Kawamura Y. Formation of 14H long period stacking ordered structure and profuse stacking faults in Mg-Zn-Gd alloys during isothermal aging at high temperature. *Acta Materialia* 2007;55(20):6798-6805.
- [57] Yamasaki M, Anan T, Yoshimoto S, Kawamura Y. Mechanical properties of warm-extruded Mg-Zn-Gd alloy with coherent 14H long periodic stacking ordered structure precipitate. *Scripta Materialia* 2005;53(7):799-803.
- [58] Yamasaki M, Izumi H, Kawamura Y, Habazaki H. Corrosion and passivation behavior of Mg-Zn-Y-Al alloys prepared by cooling-rate controlled solidification. *Applied Surface Science* 2011;257(19):8258-8267.
- [59] Haferkamp H, Boehm R, Holzkamp U, Jaschik C, Kaese V, Niemeyer M. Alloy development, processing and applications in magnesium lithium alloys. *Materials Transactions* 2001;42:1160-1166.
- [60] Wang JY, Hong WP, Hsu PC, Tan L. Microstructures and mechanical behavior of processed Mg-Li-Zn alloy. *Materials Science Forum* 2003;419-422:165-170.
- [61] Massalski T, Okamoto H, Subramanian P, Kacprzak L. Binary alloy phase diagrams. United States of America: ASM International; 2001, p.2445.
- [62] Matsuzawa K, Koshihara T, Kojima Y. Age-hardening and mechanical properties of Mg-Li-Al alloys. *Journal of Japan Institute of Light Metals* 1989;39(1):45-51.
- [63] Song JM, Wen TX, Wang JY. Vibration fracture properties of a lightweight Mg-Li-Zn alloy. *Scripta Materialia* 2007;56:529-532.
- [64] Metenier P, Gonzalez-Doncel G, Ruano OA, Wolfenstine J, Sherby DD. Superplastic behavior of a fine-grained two-phase Mg-9wt.%Li alloy. *Materials Science and Engineering A* 1990;125(2):195-202.
- [65] Sivakesavam O, Prasad YVRK. Characteristics of superplasticity domain in the processing map for hot working of as-cast Mg-11.5Li-1.5Al alloy. *Materials Science and Engineering A* 2002;323(1-2):270-277.
- [66] Dong SL, Imai T, Lim SW, Kanetake N, Saito N. Superplasticity evaluation in an Mg-8.5Li alloy. *Journal of Materials Science* 2007;42(13):5296-5298.
- [67] Cao FR, Ding H, Li YL, Zhou G, Cui JZ. Superplasticity, dynamic grain growth and deformation mechanism in ultra-light two-phase magnesium-lithium alloys. *Materials Science and Engineering A* 2010;527:2335-2341.
- [68] Liu X, Du G, Wu, R, Niu Z, Zhang M. Deformation and microstructure evolution of a strain rate superplastic Mg-Li-Zn alloy. *Journal of Alloys and Compounds* 2011;509(39):9558-9561.
- [69] Clark J, Sturkey L. The age-hardening mechanism in magnesium-lithium-zinc alloys. *The Japan Institute of Metals* 1957;86:272-276.

- [70] Alamo A, Banchik D. Precipitation phenomena in the Mg-31at% Li-1 at% Al alloy. *Journal of Materials Science* 1980;15:222-229.
- [71] Hatta H, Ramesh C, Kamado S, Kojima Y. Heat treatment characteristics and mechanical properties of superlight Mg-Li-Al alloys. *Journal of Japan Institute of Light Metals* 1997;47(4):202-207.
- [72] Saito N, Mabuchi M, Nakanishi M, Kubota K, Higashi K. The aging behavior and the mechanical properties of the Mg-Li-Al-Cu alloy. *Scripta Materialia* 1997;36:551-555.
- [73] Takuda H, Matsusaka H. Tensile properties of a few Mg-Li-Zn alloy thin sheets. *Journal of Materials Science* 2002;37:51-57.
- [74] Yamamoto A, Ashida T, Kouta Y, Kim KB, Fukumoto S, Tsubakino H. Precipitation in Mg-(4-13)%Li-(4-5)%Zn ternary alloys. *Materials Transactions* 2003;44(4):619-624.
- [75] Song GS, Staiger M, Kral M. Some new characteristics of the strengthening phase in  $\beta$ -phase magnesium-lithium alloys containing aluminum and beryllium. *Materials Science and Engineering A* 2004;371:371-376.
- [76] Hsu CC, Wang JY, Lee S. Room temperature aging characteristic of MgLiAlZn alloy. *Materials Transactions* 2008;49(11):2728-2731.
- [77] Chiu CH, Wu HY, Wang JY, Lee S. Microstructure and mechanical behavior of LZ91 Mg alloy processed by rolling and heat treatments. *Journal of Alloys and Compounds* 2008;460:246-252.
- [78] Wang PC, Lin HC, Lin KM, Yeh MT, Lin CY. A study of aging treatment on the Mg-10Li-0.5Zn alloy. *Materials Transactions* 2009;50(9):2259-2263.
- [79] Puleo DA, Huh WW. Acute toxicity of metal ions in cultures of osteogenic cells derived from bone marrow stromal cells. *Journal of Applied Biomaterials* 1995;6:109-116
- [80] Jacobs JJ, Skipor AK, Patterson LM, Hallab NJ, Paprosky WG, Black J, Galante JO. Metal release in patients who have had a primary total hip arthroplasty. A prospective, controlled, longitudinal study. *Journal of Bone Joint Surgery* 1998;80:1447-1458.
- [81] Lhotka C, Szekeres T, Steffan I, Zhuber K, Zweymuller K. Four-year study of cobalt and chromium blood levels in patients managed with two different metal-on-metal total hip replacements. *Journal of Orthopaedic Research* 2003;21:189-195.
- [82] Nagels J, Stokdijk M, Rozing PM. Stress shielding and bone resorption in shoulder arthroplasty. *Journal of Shoulder and Elbow Surgery* 2003;12:35-39.
- [83] Witte F, Fischer J, Nellesen J, Crostack HA, Kaese V, Pischd A. In vitro and in vivo corrosion measurements of magnesium alloys. *Biomaterials* 2006;27:1013-1018.
- [84] Witte F, Kaese V, Switzer H, Maeyer-Lindenberg A, Wirth CJ, Windhag H. In vivo corrosion of four magnesium alloys and the associated bone response. *Biomaterials* 2005;26:3557-3563.

- [85] Staiger MP, Pietak AM, Huadmai J, Dias G. Magnesium and its alloys as orthopedic biomaterials: a review. *Biomaterials* 2006;27:1728-1734.
- [86] Okuma T. Magnesium and bone strength. *Nutrition* 2001;17:679-680.
- [87] Vormann J. Magnesium: nutrition and metabolism. *Molecular Aspects of Medicine* 2003;24:27-37.
- [88] Revell PA, Damien E, Zhang XS, Evans P, Howlett CR. The effect of magnesium ions on bone bonding to hydroxyapatite. *Key Engineering Materials* 2004;254-256:447-450.
- [89] Zreiqat H, Howlett CR, Zannettino A, Evans P, Schulze-Tanzil G, Knabe C, et al. Mechanisms of magnesium-simulated adhesion of osteoblastic cells to commonly used orthopaedic implants. *Journal of Biomedical Materials Research* 2002;62:175-184.
- [90] Stroganov GB, Savitsky E, Mikhailovich T, Nina M, Terekhova V, Fedorovna V et al. (1972). Magnesium-base alloys for use in bone surgery. US Patent No. 3,687,135.
- [91] Li Z, Gu X, Lou S, Zheng Y. The development of binary Mg-Ca alloys for use as biodegradable materials with bone. *Biomaterials* 2008;29:1329-1344.
- [92] Gao L, Zhang C, Zhang M, Huang X, Sheng N. The corrosion of a novel Mg-11Li-3Al-0.5RE alloy in alkaline NaCl solution. *Journal of Alloys and Compounds* 2009;468: 285-289.
- [93] Zhang S, Li J, Song Y, Zhao C, Zhang X, Xie C, Zhang Y, Tao H, He Y, Jiang Y, Bian Y. In vitro degradation, hemolysis and MC3T3-E1 cell adhesion of biodegradable Mg-Zn alloy. *Materials Science and Engineering C* 2009;29:1907-1912.
- [94] Tsai MH, Chen MS, Lin LH, Lin MH, Wu CZ, Ou KL, Yu CH. Effect of heat treatment on the microstructures and damping properties of biomedical Mg-Zr alloy. *Journal of Alloys and Compounds* 2011;509:813-819.
- [95] Gray JE, Luan B. Protective coatings on magnesium and its alloys – a critical review. *Journal of Alloys and Compounds* 2002;336:88-113.
- [96] Shi Z, Song G, Atrens A. Influence of anodizing current on the corrosion resistance of anodized AZ91D magnesium alloy. *Corrosion Science* 2006;48:1939-1959.
- [97] Yu BL, Uan JY. Sacrificial Mg film anode for cathodic protection of die cast Mg-9wt.%Al-1wt.%Zn alloy in NaCl aqueous solution. *Scripta Materialia* 2006;54:1253-1257.
- [98] Ono S, Asami K, Masuko N. Mechanism of chemical conversion coating film growth on magnesium and magnesium alloys. *Materials Transactions* 2001;42:1225-1231.
- [99] Elsentriecy HH, Azumi K, Konno H. Improvement in stannate chemical conversion coatings on AZ91D magnesium alloy using the potentiostatic technique. *Electrochimica Acta* 2007;53(2):1006-1012.

- [100] Lin CS, Lee CY, Li WC, Chen YS, Fang GN. Formation of phosphate/permanganate conversion coating on AZ31 magnesium alloy. *Journal of the Electrochemical Society* 2006;153:B90-B96.
- [101] Lin JK, Hsia CL, Uan JY. Characterization of Mg,Al-hydrotalcite conversion film on Mg alloy and Cl<sup>-</sup> and CO<sub>3</sub><sup>2-</sup> anion-exchangeability of the film in a corrosive environment. *Scripta Materialia* 2007;56:527-530.
- [102] Lin JK, Uan JY. Formation of Mg,Al-hydrotalcite conversion coating on
- [103] Mg alloy in aqueous HCO<sub>2</sub><sup>-</sup>/CO<sub>3</sub><sup>2-</sup> and corresponding protection against corrosion by the coating. *Corrosion Science* 2009;51:1181-1188.
- [104] Miyata S, Okada A. Synthesis of hydrotalcite-like compounds and their physico-chemical properties. *Clays and Clay Minerals* 1977;25:14-18.
- [105] Qiu R, Iwamoto C, Satonaka S. Interfacial microstructure and strength of steel/aluminum alloy joints welded by resistance spot welding with cover plate. *Journal of Materials Processing Technology* 2009;209(8):4186-4193.
- [106] Ambroziak A, Korzeniowski M. Using resistance spot welding for joining aluminum elements in automotive. *Archives of Civil and Mechanical Engineering* 2010;10(1):5-13.
- [107] Hayat F. The effect of the welding current on heat input, nugget geometry, and the mechanical and fractural properties of resistance spot welding on Mg/Al dissimilar materials. *Materials & Design* 2011;32(4):2476-2484.
- [108] Xu W, Chen DL, Liu L, Mori H, Zhou Y. Microstructure and mechanical properties of weld-bonded and resistance spot welded magnesium-to-steel dissimilar joints. *Materials Science and Engineering A* 2012;537(1):11-24.
- [109] Kishore Babu N, Brauser S, Rethmeier M, Cross CE. Characterization of microstructure and deformation behaviour of resistance spot welded AZ31 magnesium alloy. *Materials Science and Engineering A* 2012;549(15):149-156.
- [110] Thornton PH, Krause AR, Davies RG. Aluminum spot weld. *Welding Journal* 1996;75(3):101s-108s.
- [111] Fukumoto S, Lum I, Biro E, Boomer DR, Zhou Y. Effects of electrode degradation on electrode life in resistance spot welding of aluminum alloy 5182. *Welding Journal* 2003;82(11):307s-312s.
- [112] Lang B, Sun DQ, Li GZ, Zhu BQ. Electrode degradation in resistance spot welding of magnesium alloy. *ISI International* 2009;49(11):1744-1748.
- [113] Mishra RS, Mahoney MW, McFadden SX, Mara NA, Mukherjee AK. High strain rate superplasticity in a friction stir processed 7075 Al alloy. *Scripta Materialia* 2000;42(2):163-168.

- [114] Mishra RS, Mahoney MW. Friction stir processing: A new grain refinement technique to achieve high strain rate superplasticity in commercial alloys. *Materials Science Forum* 2001;357-359:507-514.
- [115] Mishra RS, Ma ZA. Friction stir welding and processing. *Materials Science and Engineering R* 2005;50:1-78.
- [116] Jata KV, Semiatin SL. Continuous dynamic recrystallization during friction stir welding of high strength aluminum alloys. *Scripta Materialia* 2000;43(8):743-749.
- [117] Chang CI, Lee CJ, Huang JC. Relationship between grain size and Zener-Holloman parameter during friction stir processing in AZ31 Mg alloys. *Scripta Materialia* 2004;51(6):509-514.
- [118] Woo W, Choo H, Prime MB, Feng Z, Clausen B. Microstructure, texture and residual stress in a friction-stir-processed AZ31B magnesium alloy. *Acta Materialia* 2008;56(8):1701-1711.
- [119] Yu S, Chen X, Huang Z, Liu Y. Microstructure and mechanical properties of friction stir welding of AZ31B magnesium alloy added with cerium. *Journal of Rare Earths* 2010;28(2):316-320.
- [120] Chowdhury SH, Chen DL, Bhole SD, Cao X, Wanjara P. Friction stir welded AZ31 magnesium alloy: microstructure, texture, and tensile properties. *Metallurgical and Materials Transactions A – Physical Metallurgy and Materials Science* 2012; DOI: 10.1007/s11661-012-1382-3.
- [121] Hirata T, Oguri T, Hagino H, Tanaka T, Chung SW, Takigawa Y, Higashi K. Influence of friction stir welding parameters on grain size and formability in 5083 aluminum alloy. *Materials Science and Engineering* 2007;456:344-349.
- [122] Cao X, Jahazi M. Effect of welding speed on the quality of friction stir welded butt joints of a magnesium alloy. *Materials & Design* 2009;30(6):2033-2042.
- [123] Yang J, Wang D, Xiao BL, Ni DR, Ma ZY. Effects of rotation rates on microstructure, mechanical properties and fracture behavior of friction stir-welded (FSW) AZ31 magnesium alloy. *Metallurgical and Materials Transactions A – Physical Metallurgy and Materials Science* 2012;DOI:10.1007/s11661-012-1373-4.
- [124] Park SHC, Sato YS, Kokawa H. Effect of micro-texture on fracture location in friction stir weld of Mg alloy AZ61 during tensile test. *Scripta Materialia* 2003;49(2):161-166.
- [125] Park SHC, Sato YS, Kokawa H. Basal plane texture and flow pattern in friction stir weld of a magnesium alloy. *Metallurgical and Materials Transactions A – Physical Metallurgy and Materials Science* 2003;34(4):987-994.
- [126] Woo W, Choo H, Brown DW, Liaw PK, Feng Z. Texture variation and its influence on the tensile behavior of a friction-stir processed magnesium alloy. *Scripta Materialia* 2006;54:1859-1864.



- [127] Feng AH, Ma ZY. Enhanced mechanical properties of Mg-Al-Zn cast alloy via friction stir processing. *Scripta Materialia* 2007;56:397-400.
- [128] Afrin N, Chen DL, Cao X, Jahazi M. Microstructure and tensile properties of friction stir welded AZ31B magnesium alloy. *Materials Science and Engineering A* 2008;472(1-2):179-186.
- [129] Zhang DT, Suzuki M, Maruyama K. Study on the texture of a friction stir welded Mg-Al-Ca alloy. *Acta Metallurgica Sinica* 2009;48(2):335-340.
- [130] Mansoor B, Ghosh AK. Microstructure and tensile behavior of a friction stir processed magnesium alloy. *Acta Materialia* 2012;60(13-14):5079-5088.
- [131] Lathabai S, Painter MJ, Cantin GMD, TyagiVK. Friction spot joining of an extruded Al-Mg-Si alloy. *Scripta Materialia* 2006;55(10):899-902.
- [132] Chen YC, Nakata K. Friction stir lap joining aluminum and magnesium alloys. *Scripta Materialia* 2008;58(6):433-436.
- [133] Yang CW, Hung FY, Lui TS, Chen LH, Juo JY. Weibull statistics for evaluating failure behaviors and joining reliability of friction stir spot welded 5052 aluminum alloy. *Materials Transactions* 2009;50(1):145-151.
- [134] Yin YH, Ikuta A, North TH. Microstructural features and mechanical properties of AM60 and AZ31 friction stir spot welds. *Materials & Design* 2010;31(10):4764-4776.
- [135] Chen YC, Gholinia A, Prangnell PB. Interface structure and in bonding and abrasion circle friction stir spot welding: A novel approach for rapid welding aluminum alloy to steel automotive sheets. *Materials Chemistry and Physics* 2012;134(1):459-463.
- [136] Sun YF, Fujii H, Takaki N, Okitsu Y. Microstructure and mechanical properties of mild steel joints prepared by a flat friction stir spot welding technique. *Materials & Design* 2012;37:384-392.
- [137] Lin PC, Lin SH, Pan J, Pan T, Nicholson JM, Garman MA. SAE Technical Paper No. 2004-01-1330, Society of Automotive Engineering, Warrendale, PA; 2004.
- [138] Kaibyshev R, Stidikov O. Dynamic recrystallization of magnesium at ambient temperature. *Zeitschrift fuer Metallkunde* 1994;85:738-743.
- [139] McQueen HJ, Imbert CAC. Dynamic recrystallization: plastic enhancing structural development. *Journal of Alloys and Compounds* 2004;378:35-43.
- [140] Humphreys FJ, Hotherly M. *Recrystallization and Related Annealing Phenomena*. New York: Pergamon Press; 1995.
- [141] Watanabe H, Mukai T, Kohzu M, Tanabe S, Higashi K. Effect of temperature and grain size on the dominant diffusion process for superplastic flow in an AZ61 magnesium alloy. *Acta Materialia* 1999;47:3753-3758.
- [142] Lynch SP, Muddle BC, Pasang T. Ductile-to-brittle fracture transitions in 8091 Al-Li alloys. *Acta Materialia* 2001;49(15):2863-2874.

- [143] Argon AS. Mechanics and physics of brittle to ductile transitions in fracture. *Journal of Engineering Materials Technology, Transactions of the ASME* 2001;123(1):1-11.
- [144] Crocker AG, Flewitt PEJ, Smith GE. Computational modelling of fracture in polycrystalline materials. *International Materials Reviews* 2005;50(2):99-124.
- [145] Russell AM, Chumbley LS, Gantovnik VB, Xu K, Tian Y, Laabs FC. Anomalously high impact fracture toughness in BCC Mg-Li between 4.2K and 77K. *Scripta Materialia* 1998;39:1663-1667.
- [146] Counts WA, Friák M, Raabe D, Neugebauer J. Using ab initio calculations in designing bcc Mg-Li alloys for ultra-lightweight applications. *Acta Materialia* 2009;57(1):69-76.
- [147] Hughes GM, Flewitt PEJ. Temperature dependence of mechanical properties of zinc and Zircaloy measured using miniaturized disc tests. *Materials Science and Technology* 2008;24(5):567-574.
- [148] Yang CW, Lui TS, Chen LH, Hung HE. Tensile mechanical properties and failure behaviors with the ductile-to-brittle transition of the  $\alpha+\beta$ -type Mg-Li-Al-Zn alloy. *Scripta Materialia* 2009;61:1141-1144.
- [149] Bae DH, Ghosh AK. Cavity formation and early growth in a superplastic Al-Mg alloy. *Acta Materialia* 2002;50(3): 511-523.
- [150] Drozd Z, Trojanová Z, Kúdela S. Deformation behavior of Mg-Li-Al alloys. *Journal of Alloys Compounds* 2004;378(1-2):192-195.
- [151] Agnew SR, Horton JA, Yoo MH. Transmission electron microscopy investigation of  $\langle c+a \rangle$  dislocations in Mg and  $\alpha$ -solid solution Mg-Li alloys. *Metallurgical and Materials Transactions A – Physical Metallurgy and Materials Science* 2002;33(3):851-858.

IntechOpen